

---

# CONSTRUCTING COARSE-SCALE BIFURCATION DIAGRAMS FROM SPATIO-TEMPORAL OBSERVATIONS OF MICROSCOPIC SIMULATIONS: A PARSIMONIOUS MACHINE LEARNING APPROACH

---

**Galaris Evangelos**

Dipartimento di Matematica e Applicazioni “Renato Caccioppoli”  
Università degli Studi di Napoli Federico II, Naples, Italy

**Fabiani Gianluca**

Scuola Superiore Meridionale  
Università degli Studi di Napoli Federico II, Naples, Italy

**Gallos Ioannis**

School of Applied Mathematical and Physical Sciences  
National Technical University of Athens, Greece

**Kevrekidis Ioannis**

Department of Chemical and Biomolecular Engineering,  
Department of Applied Mathematics and Statistics,  
Department of Medicine  
Johns Hopkins University  
Baltimore, Maryland, USA

**Siettos Constantinos\***

Dipartimento di Matematica e Applicazioni ”Renato Caccioppoli”,  
Scuola Superiore Meridionale  
Università degli Studi di Napoli Federico II, Naples, Italy

## ABSTRACT

We address a three-tier computational approach for the construction of coarse-grained bifurcation diagrams from spatio-temporal data produced by microscopic simulators using machine learning. In the first step, we exploit manifold learning and in particular parsimonious Diffusion Maps to identify the intrinsic dimension of the manifolds where the emergent dynamics evolve and feature selection for the parametrization of these manifolds. In the second step, based on the selected features we learn the right-hand-side of the effective partial differential equations (PDEs) using two machine learning schemes, namely Feed-forward Neural Networks (FNNs) and Random Projection Networks (RPNNs). Finally, based on the learned black-box PDE model, we construct the corresponding bifurcation diagram, thus exploiting numerical bifurcation theory algorithms. For our illustrations, we implemented the proposed method to construct the one-parameter bifurcation diagram of the 1D FitzHugh-Nagumo PDEs from data generated by Lattice-Boltzman (LBM) numerical simulations.

---

\*corresponding author: constantinos.siettos@unina.it

**Keywords** Machine Learning, Feed-forward Neural Networks · Random Projection Neural Networks · Microscopic Simulations · Diffusion Maps · Feature Selection · Partial Differential Equations

## 1 Introduction

The discovery of physical laws from data and consequently the systematic analysis of their dynamics with established numerical analysis techniques, is a holy grail in the study of complex systems and has been the focus of intense research efforts over the the last decades [1, 2, 3, 4]. From the early '90s, exploiting both theoretical and technological advances researchers employed machine learning algorithms for system identification using macroscopic observations, i.e. assuming that we already know the set of coarse variables to model the underlying dynamics and the derivation of normal forms ([5, 6, 7, 8, 9, 10]). Bongard and Lipson [11] proposed a method for generating symbolic equations for nonlinear dynamical systems that can be described by ordinary differential equations from time series. Brunton et al. [12] addressed the so-called sparse identification of nonlinear dynamics (SINDy) method to obtain *explicit* data-driven PDEs from data when the good variables are known, and construct normal forms for bifurcation analysis. Wang et al. [3] addressed a physics-informed machine learning scheme based on deep learning to learn the solution operator of arbitrary PDEs. Kovachki et al. [4] addressed the concept of Neural Operators, mesh-free, infinitedimensional operators with neural networks to learn surrogate functional maps for the solution operators of PDEs.

However, for complex systems, such “good” macroscopic observables that can be used effectively for modelling the dynamics of the emergent patterns are not always directly available. Thus, such good “hidden” variables have to be identified from data. Such data can be available either directly from experiments or from detailed simulations using for example molecular dynamics, agent-based models, and Monte-Carlo methods. However, temporal simulations, are not sufficient for performing a series of tasks at the macroscopic/emergent level, such as stability analysis, design of controllers and numerical bifurcation analysis for tracing unstable branches of solutions as well as the identification of critical points in the parameter space that mark the onset of qualitatively different behaviours including e.g. catastrophic shifts. Hence, all in all, we confront with two major problems: (a) the identification of the appropriate variables that define (parametrize) the emerging (coarse-gained) dynamics, (b) the construction of models based on these variables. In the early 2000’s, the Equation-Free and Variable-Free multiscale framework [13, 14, 15, 16, 17] provided a systematic framework for the numerical analysis (stability, design of controllers, optimization, numerical bifurcation analysis) of the emergent dynamics as well as for the acceleration of microscopic simulations, by bridging the microscale where the physical laws may be known and the macroscopic scale where the emergent dynamics evolve. This bridging is achieved via the concept of the “coarse time steppers”, i.e. the construction of a black-box map on the macroscopic scale. By doing so, one can perform numerical analysis, even for microscopically large-scale systems tasks by exploiting the algorithms (toolkit) of matrix-free methods in the Krylov subspace [13, 18, 19, 20, 21, 17], thus bypassing the need to construct explicitly models in the form of PDEs. In the case when the macroscopic variables are not known a-priori, one can resort to state-of-the art manifold learning algorithms such as Diffusion maps [22, 23, 24, 25]. Over the last few years, efforts have been focused on developing physics-informed machine learning methods for solving forward and inverse problems, i.e. solution of high-dimensional multiscale problems described by PDEs and discovering hidden physics [1, 26, 27, 28, 29], thus both identifying the set to coarse observables and based on them to learn the effective PDEs. Lee et al. [29] addressed a methodology to find the right hand sides of macroscopic PDEs directly from microscopic data using Diffusion maps and Automatic Relevance Determination for selecting a good set of macroscopic variables, and Gaussian processes and artificial neural networks for modelling purposes. The approach was applied to identify a “black-box” PDE from data produced by Lattice-Boltzman simulations of the FitzHugh-Nagumo model in the parametric region where sustained oscillations arise.

In this paper, building on previous work ([29]), we exploit machine learning to perform numerical bifurcation analysis from spatio-temporal data produced by microscopic simulators. For the discovery of the appropriate set of coarse-gained variables, we use parsimonious Diffusion maps [30, 31], while for the identification of the right-hand side of the apparent coarse-grained PDE over a grid of values of the bifurcation parameter and initial conditions, we used Feed-forward neural networks (FNNs) and Random Projection Neural Networks (RPNN) in the form of Extreme Learning Machines (ELMs). For our illustrations we have used a Lattice- Boltzman simulator of the FitzHugh Nagumo (FHN) spatio-temporal dynamics. Upon training, the tracing of the coarse-grained bifurcation diagram using the machine-learning regressors was obtained by coupling the pseuso-arc-length continuation condition. The performance of the various schemes was compared to the reference bifurcation diagram obtained by finite differences of the deterministic FHN equations.

## 2 Methodology

The pipeline of our computational framework for constructing the bifurcation diagrams of the hidden coarse-scale parabolic PDEs from data coming from detailed microscopic simulations consists of three tasks: (a) identify the

coarse-scale variables from fine-scale time series using manifold learning and in particular parsimonious Diffusion maps, (b) based on the parsimonious coarse-grained variables learn the effective PDEs using machine learning and, (c) based on constructed machine learning model exploit the arsenal of numerical bifurcation analysis to systematically study the emergent dynamics of the microscopic/complex system. We assume that the emergent dynamics of the complex system under study on a domain  $\Omega \times [t_0, t_{end}] \subseteq \mathbb{R}^d \times \mathbb{R}$  can be modelled by a system, say of  $m$  parabolic PDEs of the form:

$$\frac{\partial u^{(i)}(\mathbf{x}, t)}{\partial t} \equiv u_t^{(i)} = F^{(i)}(t, \mathbf{x}, \mathbf{u}(\mathbf{x}, t), \mathcal{D}\mathbf{u}(\mathbf{x}, t), \mathcal{D}^2\mathbf{u}(\mathbf{x}, t), \dots, \mathcal{D}^\nu\mathbf{u}(\mathbf{x}, t), \boldsymbol{\varepsilon}), \quad (1)$$

$$(\mathbf{x}, t) \in \Omega \times [t_0, t_{end}], \quad i = 1, 2, \dots, m$$

where  $\mathbf{u}(\mathbf{x}) = [u^{(1)}(\mathbf{x}), \dots, u^{(m)}(\mathbf{x})]$ ,  $F^{(i)}$ ,  $i = 1, 2, \dots, m$  is a non-linear operator,  $\mathcal{D}^\nu\mathbf{u}(\mathbf{x})$  is the generic multi-index  $\nu$ -th order derivative, i.e., :

$$\mathcal{D}^\nu\mathbf{u}(\mathbf{x}) := \left\{ \frac{\partial^{|\nu|}\mathbf{u}(\mathbf{x})}{\partial x_1^{\nu_1} \dots \partial x_d^{\nu_d}} \mid |\nu| = \nu_1 + \nu_2 + \dots + \nu_d, \nu_1, \dots, \nu_d \geq 0 \right\},$$

and  $\boldsymbol{\varepsilon}$  denotes the (bifurcation) parameters of the system.

The boundary conditions read:

$$B_l^{(i)}(u^{(i)}(\mathbf{x}, t)) = h_l^{(i)}(\mathbf{x}, t) \quad \mathbf{x} \in \partial\Omega_l, \quad (2)$$

where  $\{\partial\Omega_l\}$  denotes an  $l$  partition of the boundary of  $\Omega$ , and initial conditions

$$u^{(i)}(t_0, \mathbf{x}) = u_0^{(i)}, \quad \mathbf{x} \in \Omega \quad (3)$$

The right-hand-side of the  $i$ -th PDE depends on say  $\gamma^{(i)}$  number of variables and bifurcation parameters from the set of variables  $\{\mathbf{x}, \mathbf{u}(\mathbf{x}), \mathcal{D}\mathbf{u}(\mathbf{x}), \mathcal{D}^2\mathbf{u}(\mathbf{x}), \dots, \mathcal{D}^\nu\mathbf{u}(\mathbf{x}), \boldsymbol{\varepsilon}\}$ . Let us denote this set as  $\mathcal{S}^{(i)}$ , with cardinality  $|\mathcal{S}^{(i)}| = \gamma(i)$ . Hence, at each spatial point  $\mathbf{x}_q$ ,  $q = 1, 2, \dots, M$  and time instant  $t_s$ ,  $s = 1, 2, \dots, N$  the set of features for the  $i$ -th PDE can be described by a vector  $\mathbf{z}_q(t_s) \in \mathbb{R}^{\gamma(i)}$ .

Here, we assume that such macroscopic equations in principle exist but there are not available in a closed-form. Instead, we assume that we have detailed observations from microscopic simulations from which we can compute the time and spatial derivatives of all the observables in  $N$  points in time and  $M$  points in space using e.g. finite differences. Thus, we aim to (a) identify the intrinsic dimension of the manifold on which the coarse-grained dynamics evolve, i.e. for each PDE identify  $\gamma(i)$ , and the coordinates that define the low-dimensional manifold, i.e. the sets  $\mathcal{S}^{(i)}$ , and based on them (b) identify the right-hand-side (RHS) of the the effective PDEs using machine learning. To demonstrate the proposed approach, we have chosen to use fine-scale data from Lattice-Boltzmann (LB) simulations of the coupled FitzHugh-Nagumo PDEs of activation and inhibition dynamics. Using the LB simulator, we produced data in time and space from different initial conditions and values of the bifurcation parameter. For the identification of the right coarse-scale variables that define the low-dimensional manifold on which the emergent dynamics evolve, we performed feature selection using parsimonious Diffusion Maps [30, 31]. Then, we trained the machine learning schemes to learn the right-hand-side of the coarse-grained PDEs on the low-dimensional manifold. Based on the constructed model, we performed numerical bifurcation analysis, employing the pseudo-arc-length continuation method. The performance of the data-driven scheme for constructing the coarse-grained bifurcation diagram was validated against the one computed with the PDEs using finite differences. A schematic overview of the proposed framework for the the case of two effective PDEs (as in the paradigm of FHN dynamics) is shown in Figure (1). In what follows, we first describe the parsimonious Diffusion Maps algorithm for feature selection. Then, we present the machine learning schemes used for identifying the right hand side of effective PDEs from the microscopic simulations, and finally we present the numerical results and compare the performance of the proposed scheme.

## 2.1 Parsimonious Diffusion Maps

Diffusion Maps is a non-linear manifold learning algorithm ([22, 23, 24]) that identifies a low-dimensional representation  $\mathbf{y}_i \in \mathbb{R}^\mu$  of a point  $\mathbf{z}_i \in \mathbb{R}^n$ ,  $i = 1, 2, \dots, N$  in the high dimensional space ( $\mu \ll n$ ) addressing the diffusion distance among points as the preserved metric ([24]). Diffusion Maps assume that the data lie on a smooth manifold, while it can be shown that the eigenvectors of the large normalized kernel matrices constructed from data converge to the eigenfunctions of Laplace-Beltrami operator on this manifold at the limit of infinite data ([22, 24]). The approximation of this Laplace-Beltrami operator is made by representing the weighted edges connecting nodes  $i$  and  $j$  commonly by a normalized diffusion kernel matrix  $W$  with elements:

$$w_{ij} = \exp\left(-\frac{\|\mathbf{z}_i - \mathbf{z}_j\|^2}{\sigma}\right), \quad (4)$$

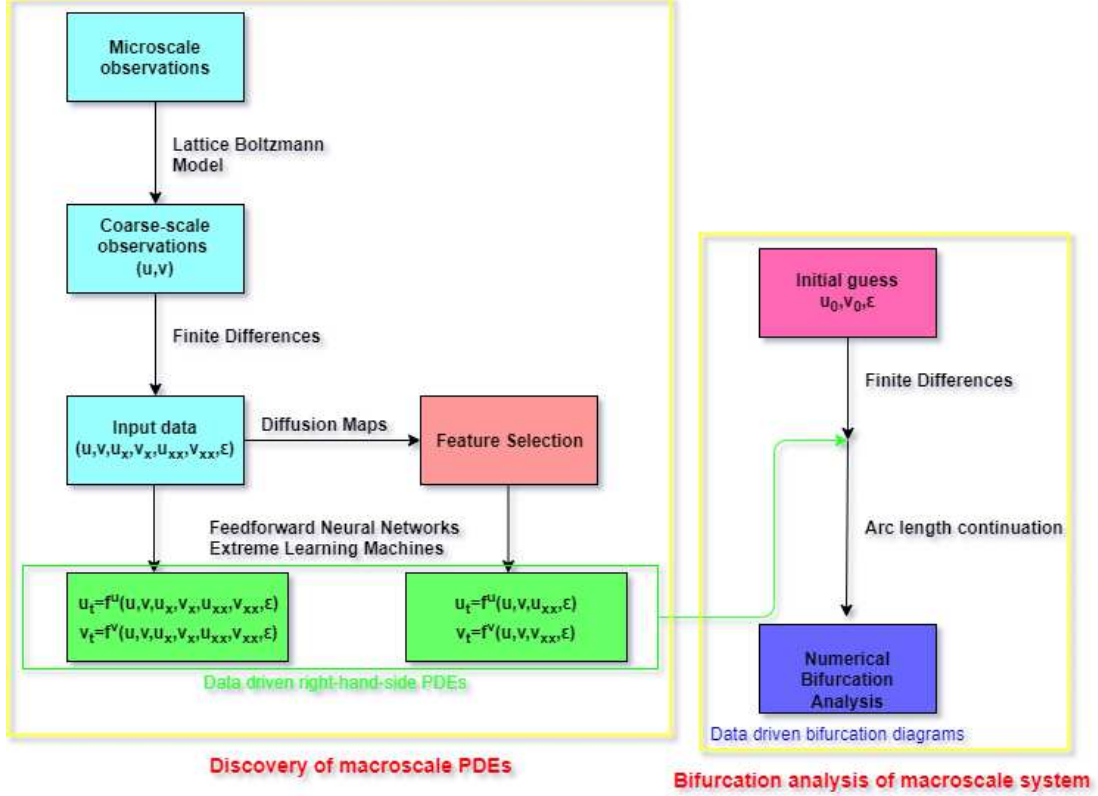


Figure 1: Schematic of the three-stage workflow for constructing coarse-grained bifurcation diagrams from fine scale observations using the paradigm of two PDEs: 1) Identify the parsimonious coarse-grained observables using Diffusion Maps from microscopic simulations (here Lattice-Boltzmann) and compute their spatial derivatives using finite differences, 2) "learn" the right hand side PDEs using machine learning algorithms (here FNNs and RPNN) and 3) employ the tools of numerical bifurcation analysis (here the pseudo arc-length continuation method to construct the coarse-grained bifurcation diagrams.

Then, one can define the  $N \times N$  diffusion matrix  $P$  by:

$$P = D^{-1}W, D = \text{diag} \left( \sum_{j=1}^N w_{ij} \right) \quad (5)$$

whose elements  $p_{ij}$  correspond to the probability of jumping from one point to another in the high-dimensional space.

Taking the power  $t$  of the diffusion matrix  $P$  is essentially identical of observing  $t$  steps forward of a Markov chain process  $Z_t$  on the data points and the element  $P^t(z_i, z_j)$  denotes the transition probability of moving from point  $i$  to point  $j$  after  $t$  steps by setting:

$$p_{ij} = p(z_i, z_j) = \text{Prob}(Z_{t+1} = z_j | Z_t = z_i). \quad (6)$$

The random walk on this weighted graph can be defined by the below transition probabilities:

$$p_{ij} = p(z_i, z_j) = \frac{w_{ij}}{\text{deg}(z_i)}, \quad (7)$$

where  $\text{deg}(z_i)$  denotes the weighted degree of the point  $i$ , defined as:

$$\text{deg}(z_i) = \sum_j w_{ij}. \quad (8)$$

At the next step it is easy to compute the so called graph Laplacian matrix  $\tilde{P}$ :

$$\tilde{P} = \tilde{D}^{1/2} P D^{-1/2}, \quad (9)$$

The eigendecomposition of  $\tilde{P}$  results to  $\tilde{P} = U\Lambda U^*$ , where  $\Lambda$  is a diagonal matrix with the eigenvalues and  $U$  is the matrix with columns the eigenvectors of  $\tilde{P}$ . The eigenvalues of  $P$  are the same of  $\tilde{P}$  since  $P$  is the adjoined of the symmetric matrix  $P$  while the left and right eigenvectors of  $P$  (say  $\Phi$  and  $\Psi$ ) are related to those of  $\tilde{P}$  as ([32]):

$$\Phi = UD^{1/2}, \quad \Psi = UD^{-1/2}. \quad (10)$$

The embedding of the manifold in  $\mu$  dimensions consists of the first  $\mu$  non-trivial/dependent eigenvectors of  $\tilde{P}$ :

$$\mathbf{y}_i = (\lambda_1^t \phi_{1,i}, \dots, \lambda_\mu^t \phi_{\mu,i}), \quad i = 1, \dots, N, \quad (11)$$

where  $t$  denotes the number of diffusion steps (usually  $t = 0$ ) and  $\lambda_1, \dots, \lambda_\mu$  the descending order eigenvalues. The diffusion distance, for two data points  $\mathbf{z}_i$  and  $\mathbf{z}_j$  at the time step  $t$  is defined as:

$$D_t^2(\mathbf{z}_i, \mathbf{z}_j) = \sum_k \frac{(p_t(\mathbf{z}_i, \mathbf{z}_k) - p_t(\mathbf{z}_j, \mathbf{z}_k))^2}{\Phi_0(\mathbf{z}_k)}, \quad (12)$$

where  $\Phi_0$  denotes the stationary distribution of the random walk described by the diffusion matrix  $P$  [33]:

$$\Phi_0(y_i) = \frac{\deg(\mathbf{z}_i)}{\sum_{\mathbf{z}_j \in Y} \deg(\mathbf{z}_j)}. \quad (13)$$

In practice, the embedding dimension  $\mu$  is determined by the spectral gap in the eigenvalues of the final decomposition. Such a numerical gap means that the first few eigenvalues would be adequate for the approximation of the diffusion distance between all pairs of points [22, 23]. Here we retain only the  $\mu$  parsimonious eigendimensions of the final decomposition as proposed in [30, 31].

### 2.1.1 Parsimonious Feature selection

Here, by identifying the coarse-scale spatio-temporal behaviour of a system of PDEs, we mean learning their right-hand sides. Hence, we first have to deal with the task of discovering the few coarse-grained spatial derivatives from the high-dimensional input data space. There exist various methods for feature selection such as LASSO ([34, 35]) or Random Forests ([36, 37]). In our framework, we used a technique that extracts the dominant features based on manifold parametrization through output-informed Diffusion Maps ([30]). The core assumption of this method is that if a given dataset in a high-dimensional, then using manifold learning algorithms (here Diffusion Maps), we can parametrize a lower-dimensional manifold.

For this purpose, given a set of  $\phi_1, \phi_2, \dots, \phi_{k-1} \in \mathbb{R}^N$  Diffusion Maps eigenvectors, for each element  $i = 1, 2, \dots, N$  of  $\phi_k$ , we use a local linear regression model:

$$\phi_{k,i} \approx \alpha_{k,i} + \beta_{k,i}^T \Phi_{k-1,i}, \quad i = 1, 2, \dots, N \quad (14)$$

to investigate if  $\phi_k$  is an dependent eigendirection;  $\Phi_{k-1,i} = [\phi_{1,i}, \phi_{2,i}, \dots, \phi_{k-1,i}^T]$ ,  $\alpha_{k,i} \in \mathbb{R}$  and  $\beta_{k,i} \in \mathbb{R}^{k-1}$ . The values of parameters  $\alpha_{k,i}$  and  $\beta_{k,i}$  are found solving an optimization problem of the form:

$$\hat{\alpha}_{k,i}, \hat{\beta}_{k,i} = \underset{\alpha, \beta}{\operatorname{argmin}} \sum_{j \neq i} K(\Phi_{k-1,i}, \Phi_{k-1,j})(\phi_{k,j} - (\alpha + \beta^T \Phi_{k-1,j}))^2 \quad (15)$$

where  $K$  is a kernel weighted function, usually the Gaussian kernel:

$$K(\Phi_{k-1,i}, \Phi_{k-1,j}) = \exp\left(-\frac{\|\Phi_{k-1,i} - \Phi_{k-1,j}\|}{\sigma^2}\right), \quad (16)$$

where  $\sigma$  is the shape parameter. The final normalized leave-one-out cross-validation (LOOCV) error for this local linear fit is defined as:

$$r_k = \sqrt{\frac{\sum_{i=1}^N (\phi_{k,i} - (\hat{\alpha}_{k,i} + \hat{\beta}_{k,i}^T \Phi_{k-1,i}))^2}{\sum_{i=1}^{\mu} (\phi_{k,i})^2}}. \quad (17)$$

For small values of  $r_k$ ,  $\phi_k$  is considered to be dependent of the other eigenvectors and hence as a harmonic or repeated eigendirection, while large values of  $r_k$ , suggest that  $\phi_k$  can serve as a new independent eigendirection.

In our application, we provide as inputs to the diffusion algorithm the combined input-output domain (the observables  $\mathbf{z}_i$  and their spatial and time derivatives). In principle, any of the subsets that is capable to parametrize the discovered embedding coordinates that were chosen after the above described methodology, can be considered as a new

possible input data domain that can be used for learning the right-hand-side PDE. We find the subsets that minimally parametrize the intrinsic embeddings by quantifying it with a total regression loss ( $L_T$ ) based on a mean squared error:

$$L_T = \left( \sum_{k=1}^{\mu} L_{\phi_k}^2 \right)^{\frac{1}{2}}. \quad (18)$$

Here, as  $L_{\phi_j}$  we define the Gaussian process regression loss ([38]) for representing the intrinsic coordinate  $\phi_j$  when using  $s$  out of  $n$  selected input features:

$$L_{\phi_k} = \frac{1}{N} \sum_{i=1}^N (\phi_{k,i} - g(\cdot))^2, \quad (19)$$

where  $g(\cdot)$  is the output of the Gaussian process regressor with inputs the values of the features in the ambient space and target values the eigenvectors  $\phi_k$ . Note that for this procedure we don't include the bifurcation parameter to the dataset. We have chosen to employ the above method separately for every subset of the same value of the bifurcation parameter and finally to select the subset of features with the minimum sum of total regression losses across all the embedding spaces.

## 2.2 Feedforward Neural Networks

It is well known that FNNs are universal approximators of any (piecewise-)continuous (multivariate) function, to any desired accuracy [39, 40, 41, 42, 43]. This implies that any failure of a function mapping by a (multilayer) network must arise from an inadequate choice of weights and biases or an insufficient number of hidden nodes. Moreover, in the univariate case only one hidden layer is needed.

Here, the output of a single hidden layer FNN that models the RHS of the  $i$ -th PDE with  $H$  hidden units at each input point  $\mathbf{z}^{(i)}(\mathbf{x}_q, t_s) \in \mathbb{R}^{\gamma^{(i)}}$ , evaluated at each point in space  $\mathbf{x}_q$ ,  $q = 1, \dots, M$ , and time  $t_s$ ,  $s = 1, 2, \dots, N$  can be written as:

$$\hat{u}_t^{(i)}(\mathbf{x}_q, t_s) = \hat{F}^{(i)}(\mathbf{z}^{(i)}(\mathbf{x}_q, t_s); \mathcal{W}^{(i)}, \mathbf{b}^{(i)}, \boldsymbol{\omega}^{o(i)}, b^{o(i)}) = \sum_{j=1}^H \omega_j^{o(i)} \psi(\boldsymbol{\omega}_j^{(i)} \cdot \mathbf{z}^{(i)}(\mathbf{x}_q, t_s) + b_j^{(i)}) + b^{o(i)}, \quad (20)$$

where  $\psi(\cdot)$  is the activation function (e.g. sigmoidal, radial basis kernel)  $\boldsymbol{\omega}^{o(i)} = (\omega_1^{o(i)}, \omega_2^{o(i)}, \dots, \omega_H^{o(i)}) \in \mathbb{R}^{1 \times H}$  are the external weights connecting the hidden layer and the output and  $b^{o(i)} \in \mathbb{R}$  is the bias of the output node, while the matrix  $\mathcal{W}^{(i)} \in \mathbb{R}^{H \times \gamma^{(i)}}$  with rows  $\boldsymbol{\omega}_j^{(i)} \in \mathbb{R}^{\gamma^{(i)}}$  and  $\mathbf{b}^{(i)} = (b_1^{(i)}, b_2^{(i)}, \dots, b_H^{(i)}) \in \mathbb{R}^H$  are the weights connecting the input and the hidden layer and the biases of the hidden layer, respectively. In the same way, one can easily extend the above explicit formula for FNNs with more than one hidden layer. Then, a loss function for each one of the  $m$  PDEs can be specified as:

$$E^{(i)} = \sum_{q=1}^M \sum_{s=1}^N (u_t^{(i)}(\mathbf{x}_q, t_s) - \hat{u}_t^{(i)}(\mathbf{x}_q, t_s))^2, \quad (21)$$

The main task of a neural network is the generalization (i.e. how good it is at learning from the given data and applying the learnt information elsewhere) and the lack of this feature is usually due to overfitting. Foresee and Hagan ([44]) showed that adding the regularization term  $E_{\omega} = \sum_{j=1}^H \omega_j^2$  to the cost function will maximize the posterior probability based on Bayes' rule. Hence, the total cost function is:

$$E_{total} = E + \lambda E_{\omega}, \quad (22)$$

where  $\lambda$  is the regularization parameter that has to be tuned. For our simulations we used the Bayesian regularized back-propagation updating the weight values through Levenberg-Marquadt optimization. ([45]).

## 2.3 Random Projection Neural Networks

Random Projection Neural Networks (RPNN) are a family of neural networks including Random Vector Functional Links (RVFLs) [46, 47], Reservoir Computing/ Echo state networks [48, 49], Extreme Learning Machines [50] and Liquid-State Networks [51]. The basic idea, which can be found in the pioneering work of Rosenblatt back in '60s [52], behind all these approaches is to use FNNs with fixed-weights between the input and the hidden layer(s), fixed biases for the nodes of the hidden layer(s), and a linear output layer. Based on that configuration, the output is projected linearly onto the functional subspace spanned by the nonlinear basis functions of the hidden layer, and the

only remaining unknowns are the weights between the hidden and the output layer. Their estimation is done by solving a nonlinear regularized least squares problem. The universal approximation properties of the RPNNs has been proved in a series of papers (see e.g. [46, 47, 49, 50]) In general the universal approximation property of random projections can be rationalized by the celebrated Johnson and Lindenstrauss (JL) Theorem: [53]:

**Theorem 1 (Johnson and Lindenstrauss)** *Let  $\mathcal{Z} \in \mathbb{R}^{n \times N}$  matrix with  $N$  points  $\mathbf{z}_i \in \mathbb{R}^n$ . Then,  $\forall \epsilon \in (0, 1)$  and  $\mu \in \mathbb{N}$  such that  $\mu \geq O(\frac{\ln N}{\epsilon^2})$ , there exists a map  $G : \mathbb{R}^n \rightarrow \mathbb{R}^\mu$  such that  $\forall \mathbf{z}_i, \mathbf{z}_j \in \mathcal{Z}$ :*

$$(1 - \epsilon)\|\mathbf{z}_i - \mathbf{z}_j\|^2 \leq \|G(\mathbf{z}_i) - G(\mathbf{z}_j)\|^2 \leq (1 + \epsilon)\|\mathbf{z}_i - \mathbf{z}_j\|^2. \quad (23)$$

Note that while the above theorem is deterministic, its proof relies on probabilistic techniques combined with Kirschbraun's theorem to yield a so-called extension mapping [53]. In particular, it can be shown that one of the many such embedding maps is simply a linear projection matrix  $R$  with entries  $r_{ij}$  that are i.i.d. random variables sampled from a normal distribution. In particular, the JL Theorem may be proved using the following lemma.

**Lemma 2** *Let  $\mathcal{Z}$  be a set of  $N$  points in  $\mathbb{R}^n$  and let  $G(\mathbf{z})$  be the random projection defined by*

$$G(\mathbf{z}) = \frac{1}{\sqrt{\mu}} R \mathbf{z}, \quad \mathbf{z} \in \mathbb{R}^n,$$

where  $R = [r_{ij}] \in \mathbb{R}^{\mu \times n}$  has components that are i.i.d. random variables sampled from a normal distribution. Then,  $\forall \mathbf{z} \in \mathcal{Z}$

$$(1 - \epsilon)\|\mathbf{z}\|^2 \leq \|G(\mathbf{z})\|^2 \leq (1 + \epsilon)\|\mathbf{z}\|^2$$

is true with probability  $p \geq 1 - 2 \exp(-(\epsilon^2 - \epsilon^3)\frac{\mu}{4})$ .

Similar proofs have been given for distributions different from the normal one (see, e.g., [54, 55, 56, 57]).

The above is a feature mapping, which may result in a dimensionality reduction ( $\mu < n$ ) or, in analogy to the case of kernel-based manifold learning methods, a projection into a higher dimensional space ( $\mu > n$ ). We also note that while the above linear random projection is but one of the choices for constructing a JL embedding, it has been experimentally demonstrated and/or theoretically proven that appropriately constructed nonlinear random embeddings may outperform simple linear random projections. For example, in [58] it was shown that deep networks with random weights for each layer result in even better approximation accuracy than the simple linear random projection.

Here we consider a random projection neural network RPNN (an ELM) with the same architecture of a single hidden layer FNN as given by Eq. (20), where  $\omega_j^{(i)}$  and  $b_j^{(i)}$  are random variables drawn from appropriate uniform distributions, the output bias  $b^o$  is set to zero, and the output weights  $\omega^{o(i)} \in \mathbb{R}^{1 \times H}$  are determined solving a linear least squares problem:

$$\hat{\mathbf{u}}_t^{(i)} = \omega^{o(i)} \mathcal{A}^{(i)}, \quad i = 1, \dots, m \quad (24)$$

where  $\hat{\mathbf{u}}_t^{(i)} \in \mathbb{R}^{MN}$  is the vector collecting all the outputs  $\hat{\mathbf{u}}_t^{(i)}(\mathbf{x}_q, t_s)$  of the RPNN for  $q = 1, \dots, M$  and  $s = 1, \dots, N$ , and the matrix  $\mathcal{A}^{(i)} \in \mathbb{R}^{H \times MN}$  is the collocation matrix which elements  $\mathcal{A}_{j,k}$  are given by:

$$\mathcal{A}_{j,k}^{(i)} = \psi(\omega_j^{(i)} \cdot \mathbf{z}_k^{(i)} + b_j^{(i)}). \quad (25)$$

where  $\mathbf{z}_k^{(i)} = \mathbf{z}^{(i)}(\mathbf{x}_q, t_s)$  and  $k = q + (s - 1)M$ . Regarding the regression problem, generally  $H \ll MN$ , thus the system (Eq. 24) is over-determined and the solution then can be computed with Singular Value Decomposition (SVD) as the resulting projection matrix  $\mathcal{A}$  is not guaranteed to be full row-rank. Given the SVD decomposition of  $\mathcal{A}$ , the pseudo inverse  $\mathcal{A}^+$  is:

$$\mathcal{A}^{(i)} = U \Sigma V^T, \quad (\mathcal{A}^{(i)})^+ = V \Sigma^+ U^T \quad (26)$$

where  $U \in \mathbb{R}^{H \times H}$  and  $V \in \mathbb{R}^{MN \times MN}$  are the unitary matrices of left and right eigenvectors respectively, and  $\Sigma \in \mathbb{R}^{H \times MN}$  is the diagonal matrix of  $H$  singular values  $\sigma_j$ . Finally, in order to regularize the problem, we can select just  $\tilde{H} < H$  singular values  $\tilde{\sigma}$  that are greater than a given tolerance, i.e.,  $\tilde{\sigma} \in \{\sigma_j \mid \sigma_j > tol, j = 1, \dots, H\}$ . Hence, the output weights  $\omega^{o(i)}$  are computed as:

$$\omega^{o(i)} = \hat{\mathbf{u}}_t^{(i)} \tilde{V} \tilde{\Sigma}^+ \tilde{U}^T. \quad (27)$$

where  $\tilde{U} \in \mathbb{R}^{H \times \tilde{H}}$ ,  $\tilde{V} \in \mathbb{R}^{MN \times \tilde{H}}$  and  $\tilde{\Sigma} \in \mathbb{R}^{\tilde{H} \times \tilde{H}}$  are restricted to the  $\tilde{\sigma}$ s.

At this point, we note that for the regression problem we aim at solving RPNNs have less flexibility than FNNs because the training is achieved using random a priori  $H$  fixed basis functions:

$$\psi_j^{(i)}(\mathbf{z}) = \psi(\omega_j^{(i)} \cdot \mathbf{z} + b_j^{(i)}), \quad (28)$$

and then the approximated function  $\hat{F}^{(i)}$  is just a linear combination of the function  $\psi_j^{(i)}$ . Note that the universal approximation theorem assure that the space generated by the basis function is dense in  $C(\mathbb{R})$  as well as  $H$  goes to infinity. While the internal function of FNN also are adapted to fit the data. Therefore here we need to find an automatically locally selection of the manifold where data lies in order to apply the RPNN properly, or in other words, we need to parsimoniously select the underling basis functions  $\{\psi_j^{(i)}\}$ . Firstly we selected as activation function the logistic sigmoid  $\psi : y \in \mathbb{R} \rightarrow \psi(y) \in \mathbb{R}$  given by:

$$\psi(y) = \frac{1}{1 + \exp(-y)}, \quad (29)$$

where, as usual in FNN,  $y$  is given by linear combination  $y = \omega_j^{(i)} \cdot \mathbf{z} + b_j^{(i)}$ . Hence the output of a neuron is given by a ridge function (a ridge function  $f : \mathbb{R}^H \rightarrow \mathbb{R}$  is such that  $f(z_1, \dots, z_n) = g(\mathbf{a}^T \cdot \mathbf{z})$ , where  $g : \mathbb{R} \rightarrow \mathbb{R}$  and  $\mathbf{a} \in \mathbb{R}^n$ ). Also we note that the inflection point of the logistic sigmoid is at  $(y = 0, \psi(y) = 1/2)$ . The points that satisfy the following relation:

$$y = \omega_j^{(i)} \cdot \mathbf{z}(\mathbf{x}_q, t_s) + b_j = 0 \quad (30)$$

form an hyperplane  $\mathcal{H}_j^{(i)}$  of  $\mathbb{R}^{MN}$  (MN dimension of  $\mathbf{z}$ ) defined by the direction  $\omega_j^{(i)}$ . Along  $\mathcal{H}_j$ ,  $\psi_j^{(i)}$  is constantly 1/2. We call the points  $c_j^{(i)} \in \mathcal{H}_j^{(i)}$  the *centers* of the ridge function  $\psi_j^{(i)}$ . Therefore is important to select the matrix  $W^{(i)}$  and  $\mathbf{b}^{(i)}$  properly in order to not have trivial (e.g., constant along the manifold  $\mathcal{M}^{(i)}$ ) generated by all the points  $\mathbf{z}(\mathbf{x}_q, t_s)$ . So we suggest to randomly sample  $H$  points  $c_j^{(i)}$  from  $(\mathbf{z}(\mathbf{x}_q, t_s))$  to be the centers of the functions  $\psi_j^{(i)}$ : in this way the inflection points of  $\psi_j^{(i)}$  lie on the manifold  $\mathcal{M}$ . Also, we independently randomly sample other  $H$  points  $\tilde{c}_j^{(i)}$  from the inputs  $(\mathbf{z}(\mathbf{x}_q, t_s))$ . Then we construct the hidden weights as:

$$\omega_j^{(i)} = \tilde{c}_j^{(i)} - c_j^{(i)}, \quad (31)$$

in order to set the direction  $\omega_j^{(i)}$  of the hyperplane  $\mathcal{H}_j^{(i)}$  parallel to the straight line that connect the two points  $\tilde{c}_j^{(i)}$  and  $c_j^{(i)}$ , so the ridge function will be constant on a direction orthogonal to the connection between two points in the manifold  $\mathcal{M}^{(i)}$  and along this line will change in value, so it will be able to discriminate the points lying on this direction. Thus, the biases  $b_j^{(i)}$  are set as:

$$b_j^{(i)} = -\omega_j^{(i)} \cdot c_j^{(i)}. \quad (32)$$

This ensures that  $c_j^{(i)} \in \mathcal{H}_j^{(i)}$  is a center of the ridge function.

### 3 Coarse-grained Bifurcation analysis based on Microscopic Simulators

For demonstrating the performance of the proposed scheme, we selected the celebrated, well studied FitzHugh-Nagumo (FHN) model first introduced in [59] to simplify the Hodgkin-Huxley model into a two-dimensional system of ODEs to describe the dynamics of the voltage across a nerve cell. In particular, we consider the FHN equations which adds a spatial diffusion term to describe the propagation of an action potential as a traveling wave. The bifurcation diagram of the one-dimensional two Partial Differential Equations (PDEs) is known to have a turning point and two supercritical Andronov-Hopf bifurcation points. In what follows, we provide the model along with the initial and boundary conditions and then we describe the microscopic simulator constructed based on the Lattice-Boltzman modeling approach.

#### 3.1 The Macroscale model: The Partial Differential Equations

The system consist in two coupled nonlinear reaction-diffusion PDEs, describing the evolution of an activator  $u : [x_0, x_{end}] \times [t_0, t_{end}] \rightarrow \mathbb{R}$  and an inhibitor  $v : [x_0, x_{end}] \times [t_0, t_{end}] \rightarrow \mathbb{R}$ :

$$\begin{aligned} \frac{\partial u}{\partial t} &= D^u \frac{\partial^2 u}{\partial x^2} + u - u^3 - v, \\ \frac{\partial v}{\partial t} &= D^v \frac{\partial^2 v}{\partial x^2} + \varepsilon(u - \alpha_1 v - \alpha_0), \end{aligned} \quad (33)$$

where  $\alpha_0$  and  $\alpha_1$  are model parameters,  $\varepsilon$  is the kinetic bifurcation parameter and  $D^u, D^v$  are the diffusion coefficients for  $u$  and  $v$  respectively. For our simulations, we set  $\alpha_1 = 2$ ,  $\alpha_0 = -0.03$ ,  $D^u = 1$ ,  $D^v = 4$  (as described in

[60]) and vary the bifurcation parameter  $\varepsilon$  in the interval  $[0.005, 0.955]$  concentrating the points at the boundary using Chebychev-Gauss-Lobatto points. We use an uniform discretization of the spatial domain  $[x_0, x_{end}] = [0, 20]$  with a step  $\Delta x = 0.2$  and of the time domain on  $[t_0, t_{end}] = [0, 450]$  with a time step  $\Delta t = 0.01$ . To solve the equation we consider Homogeneous Neumann Boundary conditions at both boundaries:

$$\begin{aligned} \frac{du}{dx}(0, t) &= 0, & \frac{dv}{dx}(0, t) &= 0, \\ \frac{du}{dx}(20, t) &= 0, & \frac{dv}{dx}(20, t) &= 0. \end{aligned} \quad (34)$$

and various initial conditions  $u_0(x) = u(x, 0)$  and  $v_0(x) = v(x, 0)$ , that, in order to explore different behaviours, we randomly select varying the following parameters of an hyperbolic tangent sigmoid:

$$\begin{aligned} u_0(x) &= w \tanh(\alpha(x - c)) + \beta \\ v_0(x) &= 0.12 \cdot u_0(x). \\ w &\sim \mathcal{U}(0.8, 1.2), & \alpha &\sim \mathcal{U}(0.5, 1) \\ c &\sim \mathcal{U}(2, 18), & \beta &\sim \mathcal{U}(-0.4, 0), \end{aligned} \quad (35)$$

where  $\mathcal{U}(a, b)$  is used to denote the uniform distribution in the interval  $[a, b]$ .

### 3.2 The Microscale simulator: the Lattice Boltzman model for the FitzHugh-Nagumo PDEs

Lattice-Boltzman modeling (LBM) ([29, 61, 62]) can be used as a mesoscopic numerical simulation for identifying spatiotemporal dynamics of finite-difference-type discretizations of the Boltzman-BGK equations ([63]). In this paper, the lattice Boltzmann model is our fine-scale ‘‘microscopic simulator’’, and its results are considered to be ‘‘the ground truth’’ from which the coarse-scale PDE and the coarse-scale bifurcation diagram will be learned.

The microscopic proprieties of atoms and molecules determine the macroscopic evolution of a physical system, but it is generally difficult to describe a system considering equations for the dynamic of each particle. The statistical description of the system at a mesoscopic level use the concept of distribution function  $f(\vec{r}, \vec{c}, t)$ , i.e.  $f(\vec{r}, \vec{c}, t)d\vec{r}d\vec{c}dt$  is the infinitesimal probability of having microscopic particles at location  $\vec{r}$  with velocities  $\vec{c}$  at a given time  $t$ , for reducing the high-number of equations and unknowns. Then, at this level, a system without an external force is governed by the Boltzmann Transport equation:

$$\frac{\partial f}{\partial t} + \vec{c} \cdot \nabla f = \mathcal{R}(f). \quad (36)$$

where the term  $\mathcal{R}(f)$  describe the rate of collisions between particles. In 1954, Bhatnagar, Gross and Krook (BGK) [64] introduced an approximation model for the collision operator:

$$\mathcal{R}(f) = \frac{1}{\tau}(f^{eq} - f), \quad (37)$$

where  $\tau$  is the so-called relaxing time coefficient and  $f^{eq}$  denote the local equilibrium distribution function.

In the LBM, the eq. (36)-(37) is collocated (assumed valid) along specific directions  $\vec{c}_i$  on a lattice:

$$\frac{\partial f_i}{\partial t} + \vec{c}_i \cdot \nabla f_i = \frac{1}{\tau}(f_i^{eq} - f_i) \quad (38)$$

and then eq. (38) is discretized, with a time step  $\Delta t$ , as follow:

$$f_i(\vec{r} + \vec{c}_i \Delta t, t + \Delta t) = f_i(\vec{r}, t) + \frac{\Delta t}{\tau}(f_i^{eq} - f_i). \quad (39)$$

One common interpretation of eq. (39) is to think about the distribution functions as fictitious particles that stream and collide along specified linkages of the lattice. Lattices are usually denoted by the notation  $DnQm$ , where  $n$  is the spatial dimension of the problem and  $m$  refer to the number of connections of each node in the lattice. The node in the lattices coincide with the points of a spatial grid with a spatial step  $\Delta x$ .

Here, in order to estimate the coarse-scale observables  $u$  and  $v$  of the FHN model, we consider the  $D1Q3$  Lattice model, i.e. we use the one-dimensional lattice with three velocities  $c_i$ : particles can stream to the right ( $c_1 = \frac{\Delta x}{\Delta t}$ ), to the left ( $c_{-1} = -\frac{\Delta x}{\Delta t}$ ) or staying still on the node ( $c_0 = 0$ ). Also we need to assume the coexistence of 2 different distribution function for describing the distribution of the activator particles  $f_i^u$  and the distribution of the inhibitor particles  $f_i^v$ , where the subscript  $i$  refer to the associated direction. Therefore, one can figure that at each instant

there are six fictitious particles on each node of the lattice: two resting on the node (with distribution  $f_0^u$  and  $f_0^v$ ), two moving on the left (with distribution  $f_{-1}^u$  and  $f_{-1}^v$ ) and two moving on the right (with distribution  $f_1^u$  and  $f_1^v$ ). The relation between the above distributions and the coarse-scale density  $u$  and  $v$  is given by the zeroth moment (across the velocity directions) of the overall distribution function:

$$\begin{aligned} u(x_j, t_k) &= \sum_{i=-1}^1 f_i^u(x_j, t_k), \\ v(x_j, t_k) &= \sum_{i=-1}^1 f_i^v(x_j, t_k). \end{aligned} \quad (40)$$

The coexistence of multiple distributions makes it necessary to introduce weights  $\omega_i$  for the connections in the lattice that should satisfy some properties:

- (a) Normalization  $\omega_0 + \omega_1 + \omega_{-1} = 1$
- (b) Symmetry  $\omega_1 - \omega_{-1} = 0$
- (c) Isotropy:
  - (c1)  $\omega_0 c_0^2 + \omega_1 c_1^2 + \omega_{-1} c_{-1}^2 = c_s^2$
  - (c2)  $\omega_0 c_0^3 + \omega_1 c_1^3 + \omega_{-1} c_{-1}^3 = 0$
  - (c3)  $\omega_0 c_0^4 + \omega_1 c_1^4 + \omega_{-1} c_{-1}^4 = 3c_s^4$

where  $c_s$  is the speed of sound in the lattice. Thus, the weights are equal to  $\omega_{\pm 1} = 1/6$  for the moving particles and  $\omega_0 = 4/6$  for the resting particle. The resulting speed of sound in the lattice is  $c_s = \frac{\sqrt{3\Delta x}}{3\Delta t}$ .

As the BGK operator (37) suggests, one key step in applying LBM for solving reaction-advection-diffusion is to determine the local equilibrium distribution function  $f^{eq}$  associated to a given model. For particles with macroscopic density  $\rho$  that move in a medium macroscopic velocity  $\vec{u}_m$ , the Maxwell distribution is:

$$\begin{aligned} f^{eq}(\vec{c}) &= \frac{\rho}{(2\pi RT)^{d/2}} \exp\left(-\frac{(\vec{c} - \vec{u}_m)^2}{2RT}\right) \\ &= \frac{\rho}{(2\pi RT)^{d/2}} \exp\left(-\frac{\vec{c} \cdot \vec{c}}{2RT}\right) \exp\left(-\frac{-2\vec{c} \cdot \vec{u}_m + \vec{u}_m \cdot \vec{u}_m}{2RT}\right) \end{aligned} \quad (41)$$

where  $d$  is the spatial dimension of the problem,  $T$  is the temperature and  $R$  is the universal gas constant. The exponential in the Eq. (41) can be expanded using Taylor series, ignoring terms of order  $O(u^3)$  and higher, obtaining:

$$f^{eq}(\vec{c}) = \rho \omega(\vec{c}) \left[ 1 + \frac{2\vec{c} \cdot \vec{u}_m - \vec{u}_m \cdot \vec{u}_m}{2c_s^2} + \frac{(\vec{c} \cdot \vec{u}_m)^2}{2c_s^4} \right] \quad (42)$$

where are used the substitutions  $\omega(\vec{c}) = (2\pi RT)^{-d/2} \exp\left(-\frac{\vec{c} \cdot \vec{c}}{2RT}\right)$  and  $RT = c_s^2$ , with  $c_s$  speed of the sound.

Now, since the FHN equation is only diffusive, i.e. there are no advection terms, the medium is stationary ( $\vec{u}_m = 0$ ) and the equilibrium distribution function, discretized on the lattice direction  $c_i$ , is simplified in:

$$\begin{aligned} f_i^{u,eq}(x_j, t_k) &= \omega_i u(x_j, t_k), \quad i = -1, 0, 1 \\ f_i^{v,eq}(x_j, t_k) &= \omega_i v(x_j, t_k). \end{aligned} \quad (43)$$

Now in the FHN model, we need to consider also a reaction terms  $R_i^l$  and so finally, the time evolution of the microscopic simulator associated to the FHN on a given  $D1Q3$  lattice is:

$$f_i^l(x_{j+i}, t_{k+1}) = f_i^l(x_j, t_k) + \frac{\Delta t}{\tau^l} (f_i^{l,eq}(x_j, t_k) - f_i^l(x_j, t_k)) + \Delta t R_i^l(x_j, t_k) \quad l \in \{u, v\} \quad (44)$$

where the superscript  $l$  denotes the activator  $u$  and the inhibitor  $v$  and the reaction terms  $R_i^l$  are directly derived by

$$\begin{aligned} R_i^u(x_j, t_k) &= \omega_i (u(x_j, t_k) - u^3(x_j, t_k) - v(x_j, t_k)), \\ R_i^v(x_j, t_k) &= \omega_i \varepsilon (u(x_j, t_k) - \alpha_1 v(x_j, t_k) - \alpha_0). \end{aligned} \quad (45)$$

Finally, the relaxation coefficient  $\frac{\Delta t}{\tau^l}$  is related to the macroscopic kinematic viscosity  $D^l$  of the FHN model and in general depends on the speed of the sound  $c_s$  associated to the lattice ([65]):

$$\frac{\Delta t}{\tau^l} = \frac{2}{1 + \frac{2}{c_s^2 \Delta t} D^l} = \frac{2}{1 + 6D^l \frac{\Delta t}{\Delta x^2}}. \quad (46)$$

We set the model parameters equals to the macro scale FHN simulator and again we vary the bifurcation parameter  $\varepsilon$  in the interval  $[0.005, 0.955]$ . The spatial and time domains also remains the same as described in the previous section and we apply homogeneous Neumann boundary conditions at both boundaries and simulate the behaviours of  $u$  and  $v$  from FHN model using the mesoscale LBM simulator.

## 4 Algorithm flow chart

Summarizing, the proposed three-tier algorithm for constructing numerically bifurcation diagram from data is provided as pseudo code in algorithm 1 and algorithm 2. In algorithm 1 the first two steps of identifying the effective coarse scale observables and learning the dynamics are shown. In algorithm 2, we describe the third step of applying the pseudo Arc-length method to the “black-box” machine learning models.

## 5 Numerical Results

### 5.1 Numerical bifurcation analysis of the FHN PDEs

For comparison purposes, we first construct the bifurcation diagram of the FHN PDEs using central Finite Differences. The discretization of the one-dimensional PDEs in  $M$  points with second-order central finite differences in the unit interval  $0 \leq x \leq 200$  leads to the following system of  $2*(M-2)$  algebraic equations  $\forall x_j = (j-1)h, j = 2, \dots, M-1$ ,  $h = \frac{1}{M-1}$ :

$$\begin{aligned} F_j^u(u, v) &= \frac{D^u}{h^2}(u_{j+1} - 2u_j + u_{j-1}) + u_j - u_j^3 - v_j = 0 \\ F_j^v(u, v) &= \frac{D^v}{h^2}(v_{j+1} - 2v_j + v_{j-1}) + \varepsilon(u_j - \alpha_1 v_j - \alpha_0) = 0. \end{aligned}$$

At the boundaries, we imposed homogeneous von Neumann boundary conditions. The above  $2*(M-2)$  nonlinear algebraic equations are solved iteratively using Newton’s method. The non-null elements of the Jacobian matrix are given by:

$$\begin{aligned} \frac{\partial F_j^u}{\partial u_{j-1}} &= \frac{D^u}{h^2}; \frac{\partial F_j^u}{\partial u_j} = -D^u \frac{2}{h^2} - 3u_j^2; \frac{\partial F_j^u}{\partial u_{j+1}} = \frac{D^u}{h^2}; \frac{\partial F_j^u}{\partial v_j} = -1 \\ \frac{\partial F_j^v}{\partial v_{j-1}} &= \frac{D^v}{h^2}; \frac{\partial F_j^v}{\partial v_j} = -D^v \frac{2}{h^2} - \varepsilon \alpha_1 v_j; \frac{\partial F_j^v}{\partial v_{j+1}} = \frac{D^v}{h^2}; \frac{\partial F_j^v}{\partial u_j} = \varepsilon. \end{aligned}$$

To trace the solution branch along the critical points, we used the “pseudo” arc-Length-continuation method ([66, 67, 68]). This involves the parametrization of  $u(x)$ ,  $v(x)$  and  $\varepsilon(x)$  by the arc-length  $s$  on the solution branch. The solution is sought in terms of  $\tilde{u}(x, s)$ ,  $\tilde{v}(x, s)$  and  $\tilde{\varepsilon}(s)$  in an iterative manner, by solving until convergence the following augmented system:

$$\begin{bmatrix} \nabla_u \mathbf{F}^u & \nabla_v \mathbf{F}^u & \nabla_\varepsilon \mathbf{F}^u \\ \nabla_u \mathbf{F}^v & \nabla_v \mathbf{F}^v & \nabla_\varepsilon \mathbf{F}^v \\ \nabla_u \mathbf{N} & \nabla_v \mathbf{N} & \nabla_\varepsilon \mathbf{N} \end{bmatrix} \begin{bmatrix} du^{(n)}(x, s) \\ dv^{(n)}(x, s) \\ d\varepsilon^{(n)}(s) \end{bmatrix} = - \begin{bmatrix} \mathbf{F}^u(u^{(n)}(x, s), v^{(n)}(x, s), \varepsilon^{(n)}(s)) \\ \mathbf{F}^v(u^{(n)}(x, s), v^{(n)}(x, s), \varepsilon^{(n)}(s)) \\ \mathbf{N}(u^{(n)}(x, s), v^{(n)}(x, s), \varepsilon^{(n)}(s)) \end{bmatrix}, \quad (47)$$

where

$$\nabla_\varepsilon \mathbf{F}^u = \left[ \frac{\partial F_1^u}{\partial \varepsilon} \quad \frac{\partial F_2^u}{\partial \varepsilon} \quad \dots \quad \frac{\partial F_M^u}{\partial \varepsilon} \right]^T, \quad \nabla_\varepsilon \mathbf{F}^v = \left[ \frac{\partial F_1^v}{\partial \varepsilon} \quad \frac{\partial F_2^v}{\partial \varepsilon} \quad \dots \quad \frac{\partial F_M^v}{\partial \varepsilon} \right]^T,$$

and

$$\begin{aligned} \mathbf{N}(u^{(n)}(x, s), v^{(n)}(x, s), \varepsilon^{(n)}(s)) &= \\ (u^{(n)}(x, s) - \tilde{u}(x, s))_2^T \cdot \frac{(\tilde{u}(x)_{-2} - \tilde{u}(x)_{-1})}{ds} &+ \\ (v^{(n)}(x, s) - \tilde{v}(x, s))_2^T \cdot \frac{(\tilde{v}(x)_{-2} - \tilde{v}(x)_{-1})}{ds} &+ \\ (\varepsilon^{(n)}(s) - \tilde{\varepsilon}(s)) \cdot \frac{(\tilde{\varepsilon}_{-2} - \tilde{\varepsilon}_{-1})}{ds} - ds, & \end{aligned}$$

---

**Algorithm 1** Identify the coarse scale observables from fine scale observations and learn the coarse dynamics for the FHN PDEs.

---

!

**Require:** Grid  $N_\varepsilon$  of Chebysev-Gauss-Lobatto points in  $[0.005, 0.955]$  for  $\varepsilon$   $\triangleright$  set grid for bifurcation parameter  $\varepsilon$

**Require:**  $\mathbf{x} = [x_0 : \Delta x : x_{end}]$  and  $\mathbf{t} = [t_0 : \Delta t : t_{end}]$  be the space and time grid with  $M$  and  $N$  points respectively

1:  $inits \leftarrow N_i$   $\triangleright$  set # of initial conditions

2. **1. Identify the coarse scale observables.**

2:  $L_t^u \leftarrow 0, L_t^v \leftarrow 0$

3: **for**  $\varepsilon = 1, \dots, N_\varepsilon$  **do**

4:   **for**  $i = 1, \dots, N_i$  **do**

5:     Select  $w \sim \mathcal{U}(0.8, 1.2), c \sim \mathcal{U}(2, 18),$   
 $\alpha \sim \mathcal{U}(0.5, 1), \beta \sim \mathcal{U}(-0.4, 0).$

6:      $u_i(\mathbf{x}, 0, \varepsilon) \leftarrow wtanh(\alpha(\mathbf{x} - c)) + \beta$

7:      $v_i(\mathbf{x}, 0, \varepsilon) \leftarrow 0.12 \cdot u_i(\mathbf{x}, 0, \varepsilon)$   $\triangleright$  see equation 35

8:     **for**  $s = 2 : N$  **do**

9:        $f_j^{u, eq}(\mathbf{x}, \mathbf{t}(s), \varepsilon) \leftarrow \omega_j u(\mathbf{x}, \mathbf{t}(s), \varepsilon), j = -1, 0, 1$

10:        $f_j^{v, eq}(\mathbf{x}, \mathbf{t}(s), \varepsilon) \leftarrow \omega_j v(\mathbf{x}, \mathbf{t}(s), \varepsilon), j = -1, 0, 1$   $\triangleright$  see equation 43

11:        $u_i(\mathbf{x}, \mathbf{t}(s), \varepsilon) \leftarrow \sum_{j=-1}^1 f_j^{u, eq}(\mathbf{x}, \mathbf{t}(s), \varepsilon)$

12:        $v_i(\mathbf{x}, \mathbf{t}(s), \varepsilon) \leftarrow \sum_{j=-1}^1 f_j^{v, eq}(\mathbf{x}, \mathbf{t}(s), \varepsilon)$   $\triangleright$  see equation 40

13:       Compute  $u_{t,i}, v_{t,i}, u_{x,i}, v_{x,i}, u_{xx,i}, v_{xx,i}$   $\triangleright$  using central finite differences.

14:     **end for**

15:   **end for**

16:  Compute the first  $\mu$  Diffusion Maps (DM) eigenvectors:

17:   $[\phi_1^u, \dots, \phi_\mu^u] \leftarrow \text{DM}(u, v, u_t, u_x, v_x, u_{xx}, v_{xx})$   $\triangleright$  see equation 11

18:   $[\phi_1^v, \dots, \phi_\mu^v] \leftarrow \text{DM}(u, v, v_t, u_x, v_x, u_{xx} v_{xx})$

19:   $z \leftarrow [u, v, u_x, v_x, u_{xx}, v_{xx}]$

20:  **for** every  $q \subset z$  **do**

21:   **for**  $k = 1, \dots, \mu$  **do**

22:      $\hat{\phi}_k^u \leftarrow GP(q)$

23:      $\hat{\phi}_k^v \leftarrow GP(q)$   $\triangleright$  GP: Gaussian process regressor

24:      $L_{\phi_k^u} \leftarrow \frac{1}{N} \sum_{i=1}^N (\phi_{k,i}^u - \hat{\phi}_k^u)^2$

25:      $L_{\phi_k^v} \leftarrow \frac{1}{N} \sum_{i=1}^N (\phi_{k,i}^v - \hat{\phi}_k^v)^2$   $\triangleright$  see equation 19

26:   **end for**

27:    $L_t^u(q) \leftarrow L_t^u(q) + (\sum_{j=1}^\mu L_{\phi_j^u}^2)^{\frac{1}{2}}$

28:    $L_t^v(q) \leftarrow L_t^v(q) + (\sum_{j=1}^\mu L_{\phi_j^v}^2)^{\frac{1}{2}}$   $\triangleright$  see equations 18 and 19

29:  **end for**

30:  **end for**

31:   $z_u \leftarrow \{q^* : L_t^u(q^*) = \min(L_t^u)\}$

32:   $z_v \leftarrow \{q^* : L_t^v(q^*) = \min(L_t^v)\}$   $\triangleright$  extract the effective features

33. **2. Learn the coarse scale PDEs**

34: Train two FNNs/RPNNs without feature selection:

35:  $\hat{F}^u \equiv \hat{u}_t \leftarrow \text{FFN/RPNN}(\mathbf{z}, \varepsilon)$

36:  $\hat{F}^v \equiv \hat{v}_t \leftarrow \text{FFN/RPNN}(\mathbf{z}, \varepsilon)$   $\triangleright$  without feature selection

37: Train two FNNs/RPNNs with feature selection:

38:  $\hat{F}_r^u \equiv \hat{u}_{t,r} \leftarrow \text{FFN/RPNN}(z_u, \varepsilon)$

39:  $\hat{F}_r^v \equiv \hat{v}_{t,r} \leftarrow \text{FFN/RPNN}(z_v, \varepsilon)$   $\triangleright$  with feature selection

---

**Algorithm 2** Construct bifurcation diagrams with pseudo-arc-length continuation method.

---

**3. Wrap around the machine learning model the pseudo Arc-Length method.**

```

1:  $\varepsilon_0 \leftarrow 0.005, \varepsilon_{-2} \leftarrow \varepsilon_0, \varepsilon_{-1} \leftarrow \varepsilon_{-2} + 5e - 04$ 
2:  $u_0 \leftarrow -\tanh(0.5(\mathbf{x} - 9.5)), v_0 = 0.12u_0$   $\triangleright$  set initial guesses
3:  $[u_{-2}; v_{-2}] \leftarrow \text{NR}(u_0, v_0, \varepsilon_{-2})$ 
    $[u_{-1}; v_{-1}] \leftarrow \text{NR}(u_0, v_0, \varepsilon_{-1})$   $\triangleright$  approximate the solutions for the first step with Newton Raphson
4:  $\zeta_{-2} \leftarrow [u_{-2}; v_{-2}; \varepsilon_{-2}], \zeta_{-1} \leftarrow [u_{-1}; v_{-1}; \varepsilon_{-1}]$ 
5:  $\text{maxiter} \leftarrow 6$   $\triangleright$  set max # iters for Newton method
6:  $\delta = 1e - 06$   $\triangleright$  perturbation parameter
7:  $\text{tol} = 1e - 06$ 
8: repeat
9:    $\Delta s = \sqrt{\text{sum}((\zeta_{-1}(1:2) - \zeta_{-2}(1:2))^2 + (\zeta_{-1}(3) - \zeta_{-2}(3))^2}$ 
10:   $\zeta \leftarrow 2\zeta_{-1} - \zeta_{-2}$ 
11:   $\mathbf{N} \leftarrow \frac{\zeta_{-1}(1:2) - \zeta_{-2}(1:2)}{\Delta s} + \frac{\zeta_{-1}(3) - \zeta_{-2}(3)}{\Delta s}$ 
12:   $\text{iter} \leftarrow 0$ 
13:  repeat
14:    for  $j = 1, \dots, M$  do
15:       $\frac{\partial \hat{F}^u}{\partial u_j} \leftarrow \frac{\hat{F}^u(u_j, v_j, \varepsilon) - \hat{F}^u(u_j + \delta, v_j, \varepsilon)}{2\delta}; \frac{\partial \hat{F}^u}{\partial v_j} \leftarrow \frac{\hat{F}^u(u_j, v_j, \varepsilon) - \hat{F}^u(u_j, v_j + \delta, \varepsilon)}{2\delta}$ 
          $\frac{\partial \hat{F}^v}{\partial u_j} \leftarrow \frac{\hat{F}^v(u_j, v_j, \varepsilon) - \hat{F}^v(u_j + \delta, v_j, \varepsilon)}{2\delta}; \frac{\partial \hat{F}^v}{\partial v_j} \leftarrow \frac{\hat{F}^v(u_j, v_j, \varepsilon) - \hat{F}^v(u_j, v_j + \delta, \varepsilon)}{2\delta}$ 
          $\frac{\partial \hat{F}^u}{\partial \varepsilon} \leftarrow \frac{\hat{F}^u(u_j, v_j, \varepsilon) - \hat{F}^u(u_j, v_j, \varepsilon + \delta)}{2\delta}; \frac{\partial \hat{F}^v}{\partial \varepsilon} \leftarrow \frac{\hat{F}^v(u_j, v_j, \varepsilon) - \hat{F}^v(u_j, v_j, \varepsilon + \delta)}{2\delta}$ 
          $\frac{\partial \mathbf{N}}{\partial u_j}; \frac{\partial \mathbf{N}}{\partial v_j}; \frac{\partial \mathbf{N}}{\partial \varepsilon}$ 
16:    end for
17:    Compute the Jacobian  $\nabla \mathbf{F} \leftarrow \begin{bmatrix} \nabla_u \hat{F}^u & \nabla_v \hat{F}^u & \nabla_\varepsilon \hat{F}^u \\ \nabla_u \hat{F}^v & \nabla_v \hat{F}^v & \nabla_\varepsilon \hat{F}^v \\ \nabla_u \mathbf{N} & \nabla_v \mathbf{N} & \nabla_\varepsilon \mathbf{N} \end{bmatrix}$   $\triangleright$  see eq 47
18:     $\Delta \zeta \leftarrow (\nabla \mathbf{F})^\dagger \mathbf{F}$ 
19:     $\zeta \leftarrow \zeta - \Delta \zeta$   $\triangleright$  update solutions
20:     $\text{err} \leftarrow \|\mathbf{F}\|_2$   $\triangleright$  compute error
21:     $\text{iter} \leftarrow \text{iter} + 1$ 
22:  until  $(\text{err} \leq \text{tol})$  or  $(\text{iter} \geq \text{maxiter})$ 
23:   $\zeta_{-2} \leftarrow \zeta_{-1}, \zeta_{-1} \leftarrow \zeta$ 
24:   $\tilde{u} \leftarrow \zeta(1), \tilde{v} \leftarrow \zeta(2), \tilde{\varepsilon} \leftarrow \zeta(3)$ 
25: until  $\tilde{\varepsilon} < \varepsilon_0$ 

```

---

where  $(\tilde{u}(x)_{-2}, \tilde{v}(x)_{-2})$  and  $(\tilde{u}(x)_{-1}, \tilde{v}(x)_{-1})$  are two already found consequent solutions for  $\tilde{\varepsilon}_{-2}$  and  $\tilde{\varepsilon}_{-1}$ , respectively and  $ds$  is the arc-length step for which a new solution around the previous solution  $(\tilde{u}(x)_{-2}, \tilde{v}(x)_{-2}, \tilde{\varepsilon}_{-2})$  along the arc-length of the solution branch is being sought. The corresponding bifurcation diagram is shown in Figure 2. We obtained a Andronov-Hopf bifurcation at  $\varepsilon \approx 0.018497$  and a fold point at  $\varepsilon \approx 0.95874$ . This is considered as the reference bifurcation diagram.

## 5.2 Numerical bifurcation analysis from Microscopic Simulations

For  $u(x, t)$  and  $v(x, t)$ , we collected transients with a sampling rate of 1s, from 10 different random sampled initial conditions for 40 different values for the bifurcation parameter ( $\varepsilon$ ). In particular, we created a grid of 40 different  $\varepsilon$  in  $[0.005, 0.955]$  using Gauss-Chebychev-Lobatto points, while the 10 initial conditions are sampled according to Eq.35. Figure 4) depicts the total of 400 training initial conditions. Thus, we end up with a dataset consisting of 40 (values of  $\varepsilon$ ) $\times$ 10 (initial conditions) $\times$ 448 (time points ignoring the first 2s of the transient) $\times$ 40 (space points)  $\simeq 7.168.000$  data points.

For learning the coarse-grained dynamics and construct the corresponding bifurcation diagram, we trained two FNNs and two RPNNs (one for each one of the variables  $u$  and  $v$ ).

The FNNs were constructed using two hidden layers with 12 units each. Hidden units were employed with the hyperbolic tangent sigmoid activation function while the regularization parameter was tuned and set  $\lambda = 0.01$ . For the training of the FNNs we used the Deep Learning toolbox of MATLAB 2021a on an Intel Core i5-8265U with up to 3.9 GHz frequency and a memory of 8 GB.

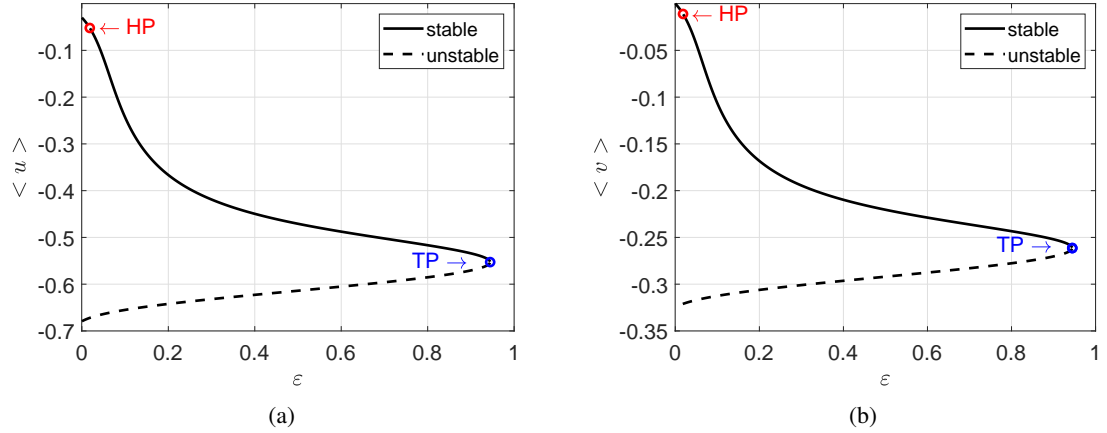


Figure 2: Reference bifurcation diagram of the FHN PDEs with respect to  $\epsilon$  as computed with FD and  $N = 200$  points. (a)  $\langle u \rangle$ , (b)  $\langle v \rangle$ . Andronov-Hopf Point:  $HP_\epsilon = 0.01827931$ . Turning Point:  $TP_\epsilon = 0.94457768$ .

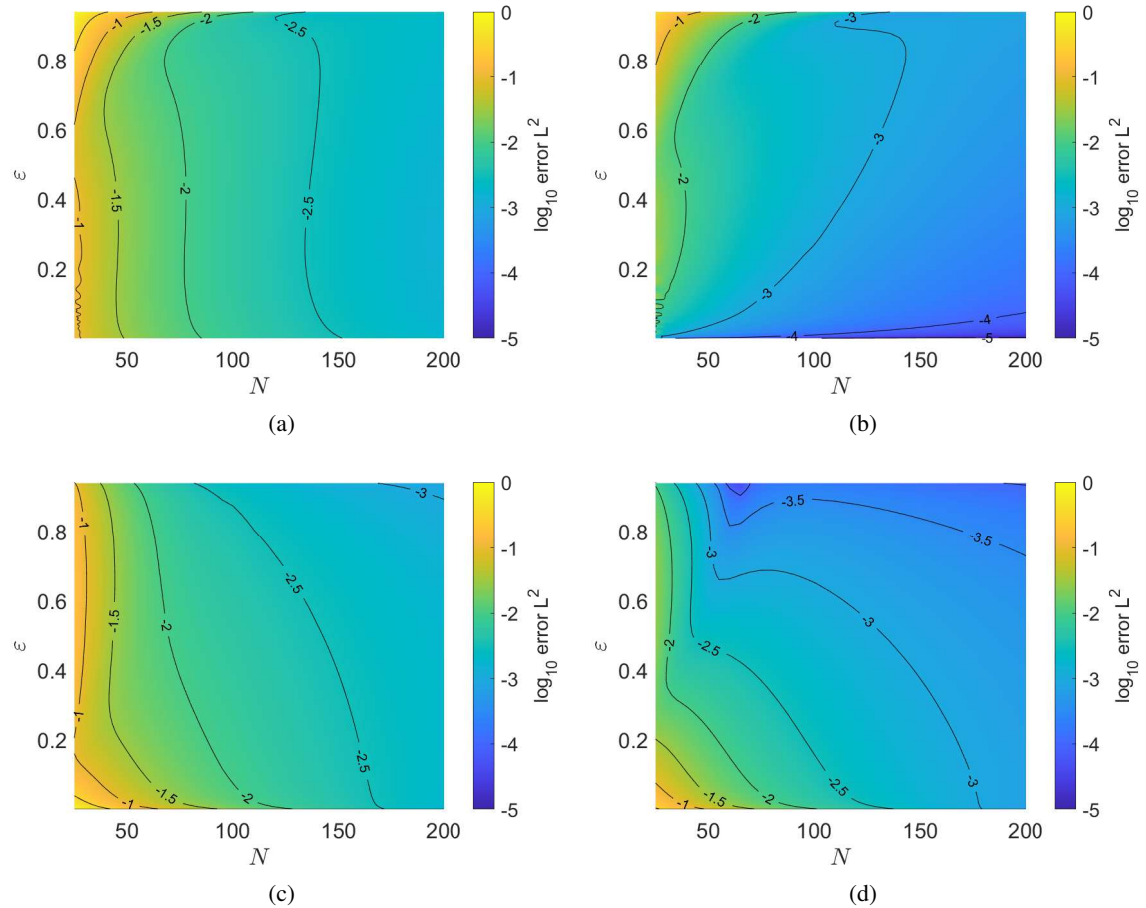


Figure 3: Contour plot of the  $L_2$  norm of the convergence of the solutions as computed with Finite Differences with respect to the size of the grid  $N$  as  $L2_N = \|u_N - u_{2N}\|_2$ . The convergence error was evaluated on 1001 grid points, using linear piecewise interpolation. (a) upper branch for  $u$  (b) upper branch for  $v$  (c) lower branch for  $u$  (d) lower branch for  $v$ .

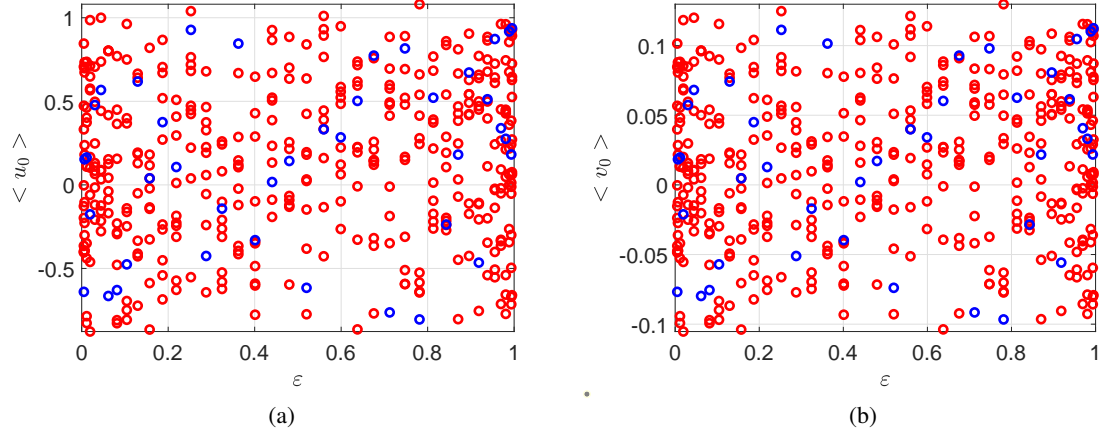


Figure 4: Coarse initial conditions for (a)  $u$  and (b)  $v$  for the training. Every dot denotes a point whose  $\varepsilon$  and mean  $u$  (or  $v$ ) were used for input data. Red dots are training points, blue points are testing points. The grid is spanned with Chebychev-Gauss-Lobatto points for epsilons in the interval  $[0.005, 0.995]$  and the initial condition are randomly selected as in Eq. (35)

### 5.2.1 Numerical bifurcation analysis without feature selection

In Figures(5(a)),(5(b)), we show the regression performance in the test dataset of the FNNs and RPNNs, respectively. Table (1) summarises the performance of the two schemes on the training and on test data set. The training phase of the FNN for  $\hat{u}_t$  stopped at 828-th epoch and required around 4 hours with minimum tolerance set to  $1e - 07$ . The training phase of the FNN for  $\hat{v}_t$  stopped at 1000-th epoch and required around 4h with minimum tolerance set to  $1e - 10$ . Differences between the predicted and the actual values of the time derivatives of  $u$  and  $v$  for three different values of  $\varepsilon$  are shown in Figure (6). Instead, the training phase of the RPNNs for  $\hat{u}_t$  and  $\hat{v}_t$  required around 8 minutes each in matlab R2020b using a single core of an Intel i7-10750H CPU @ 2.60GHz and 16GB RAM, thus resulting to a training phase at least 20 times faster.

After training, we used the FNNs and RPNNs to compute with finite differences the quantities required for performing the bifurcation analysis (see Eq.(47)), i.e.:

$$\begin{aligned} \frac{\partial \hat{F}^u}{\partial u_j} &= \frac{\hat{F}^u(u_j, v_j, \varepsilon) - \hat{F}^u(u_j + \delta, v_j, \varepsilon)}{2\delta}; \quad \frac{\partial \hat{F}^u}{\partial v_j} = \frac{\hat{F}^u(u_j, v_j, \varepsilon) - \hat{F}^u(u_j, v_j + \delta, \varepsilon)}{2\delta} \\ \frac{\partial \hat{F}^v}{\partial u_j} &= \frac{\hat{F}^v(u_j, v_j, \varepsilon) - \hat{F}^v(u_j + \delta, v_j, \varepsilon)}{2\delta}; \quad \frac{\partial \hat{F}^v}{\partial v_j} = \frac{\hat{F}^v(u_j, v_j, \varepsilon) - \hat{F}^v(u_j, v_j + \delta, \varepsilon)}{2\delta} \\ \frac{\partial \hat{F}^u}{\partial \varepsilon} &= \frac{\hat{F}^u(u_j, v_j, \varepsilon) - \hat{F}^u(u_j, v_j, \varepsilon + \delta)}{2\delta}; \quad \frac{\partial \hat{F}^v}{\partial \varepsilon} = \frac{\hat{F}^v(u_j, v_j, \varepsilon) - \hat{F}^v(u_j, v_j, \varepsilon + \delta)}{2\delta}, \end{aligned}$$

with  $\delta = 1e - 06$ . The reconstructed bifurcation diagrams are shown in Figure (11). Using the FNNs, we estimated the Andronov-Hopf point at  $\varepsilon \approx 0.0191$  and the turning point at  $\varepsilon \approx 0.9713$ ; using the RPNNs, we estimated the Andronov-Hopf point at  $\varepsilon \approx 0.0193$  and the turning point at  $\varepsilon \approx 0.9696$ . We approximated the same points using the finite differences scheme in the previous section at  $\varepsilon \approx 0.0183$  for the Andronov-Hopf point and at  $\varepsilon \approx 0.9446$  for the turning point.

### 5.3 Numerical bifurcation analysis with feature selection

Here, we aimed at identifying if any subset of features of the input domain can be used for parametrizing the intrinsic embeddings (and thus learn the RHS of the PDEs). We applied Diffusion Maps for every sample of the test dataset with the same value of the bifurcation parameter and identified the three parsimonious leading eigenvectors as described in section 2.1. We denote them as  $\phi_1, \phi_2, \phi_3$ . We have set the width parameter of the Gaussian kernel to  $\sigma = 10$ . The three parsimonious Diffusion Maps coordinates for different values of the parameter epsilon are shown in figure (10). For  $\varepsilon = 0.114$  that is close to the Andronov-Hopf point, the embedded space is a two dimensional “carpet” in the three dimensional space. The oscillatory behaviour leads to different values of the time derivative which can be effectively parametrized as shown by the coloring of the manifold (Figures 10(a), 10(b)). On the contrary, for  $\varepsilon = 0.4010$  and

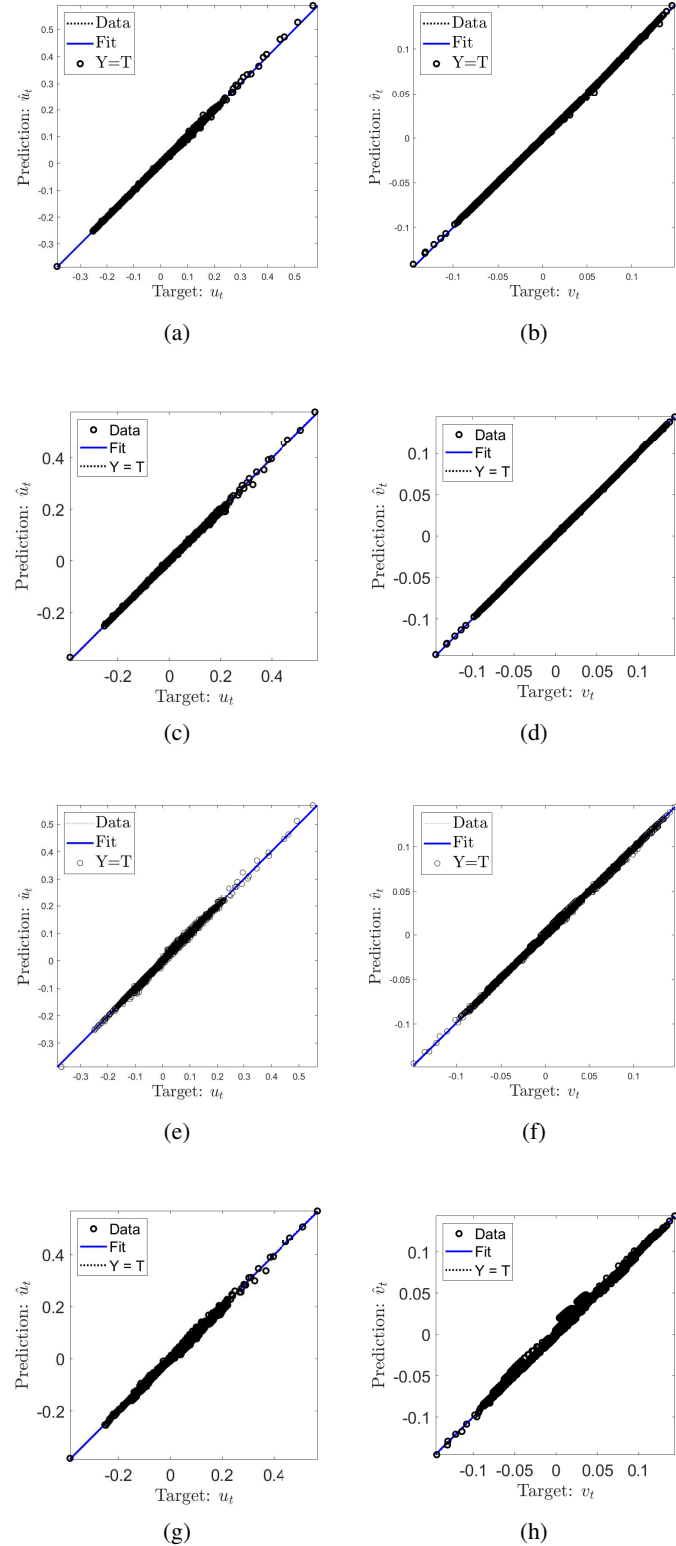


Figure 5: Regression results for the test dataset of the two schemes (FNNs and RPNNs): (a) FNN without feature selection ( $R=0.99996$ ), (b) FNN without feature selection ( $R=0.99992$ ), (c) RPNN without feature selection ( $R=0.99985$ ), (d) ELM without feature selection ( $R=0.99998$ ). (e) FNN with feature selection ( $R=0.99712$ ), (f) FNN with feature selection ( $R=0.99950$ ), (g) ELM with feature selection ( $R=0.99962$ ), (h) ELM with feature selection ( $R=0.99914$ ).

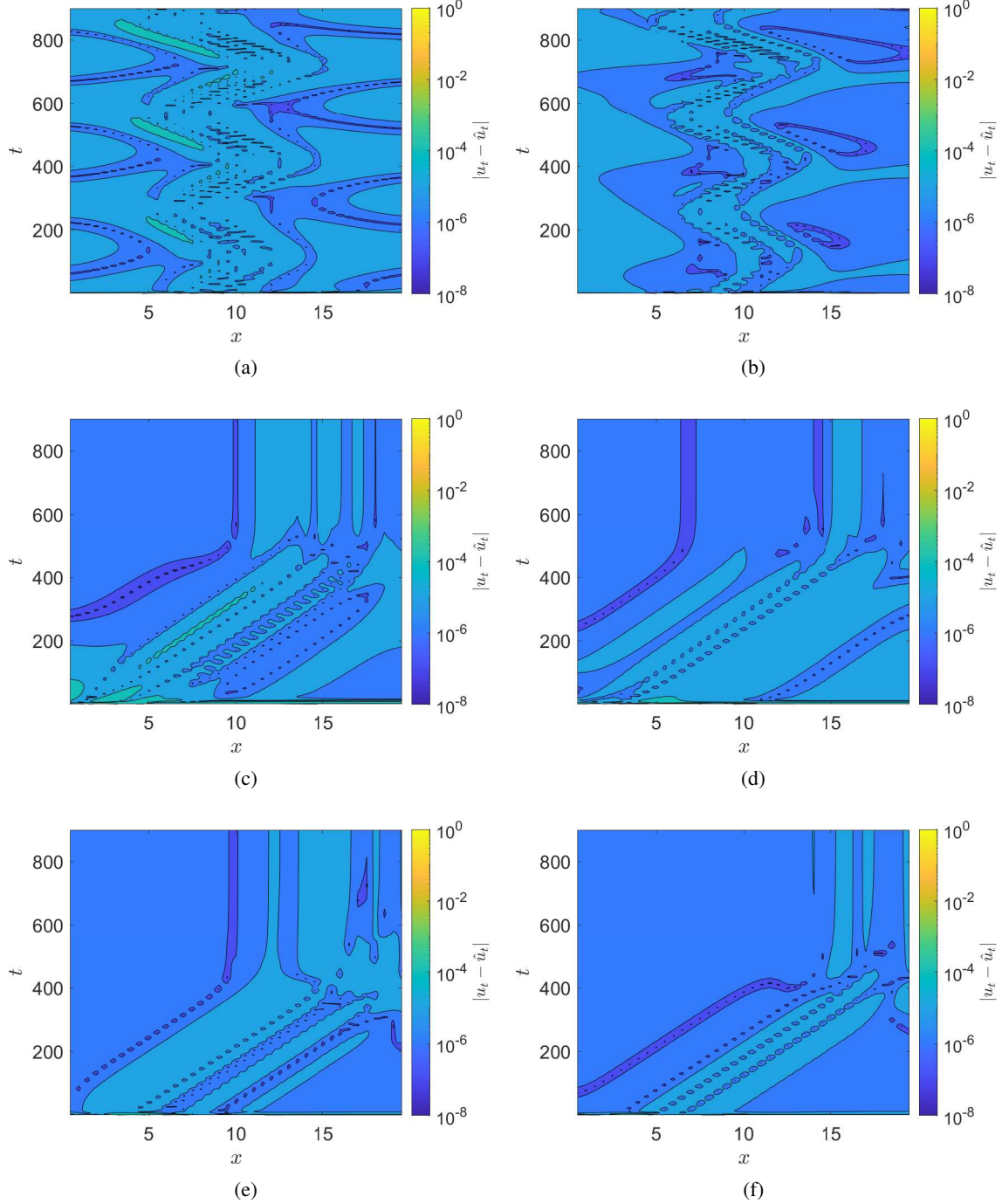


Figure 6: Contour plot for  $\|u_t - \hat{u}_t\|$  in the test dataset between the predicted time derivatives from the FNNs ( $\hat{u}_t$ ) without feature selection and the actual time derivatives  $u_t$  ((a), (c), and (e)) and for  $\|v_t - \hat{v}_t\|$  ((b), (d), and (f)) for different values of  $\varepsilon$ : (a) and (b)  $\varepsilon = 0.0114$  near the Andronov-Hopf point, (c), (d)  $\varepsilon = 0.4$ , (e) and (f)  $\varepsilon = 0.9383$  near the turning point.

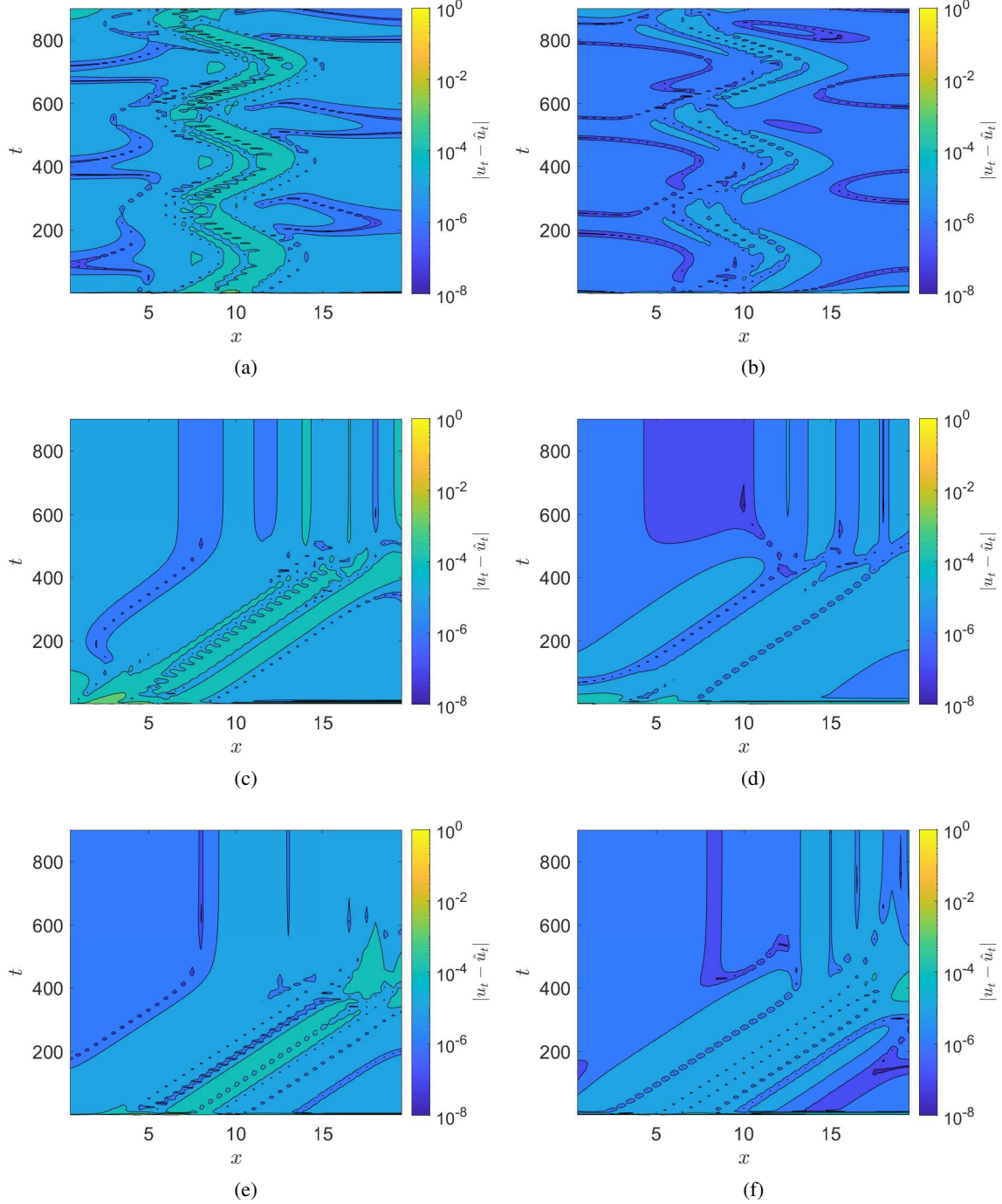


Figure 7: Contour plot for  $\|u_t - \hat{u}_t\|$  in the test dataset between the predicted time derivatives from the FNNs ( $\hat{u}_t$ ) with feature selection and the actual time derivatives  $u_t$  ((a), (c), and (e)) and for  $\|v_t - \hat{v}_t\|$  ((b), (d), and (f)) for different values of  $\varepsilon$ : (a) and (b)  $\varepsilon = 0.0114$  near the Andronov-Hopf point, (c), (d)  $\varepsilon = 0.4$ , (e) and (f)  $\varepsilon = 0.9383$  near the turning point.

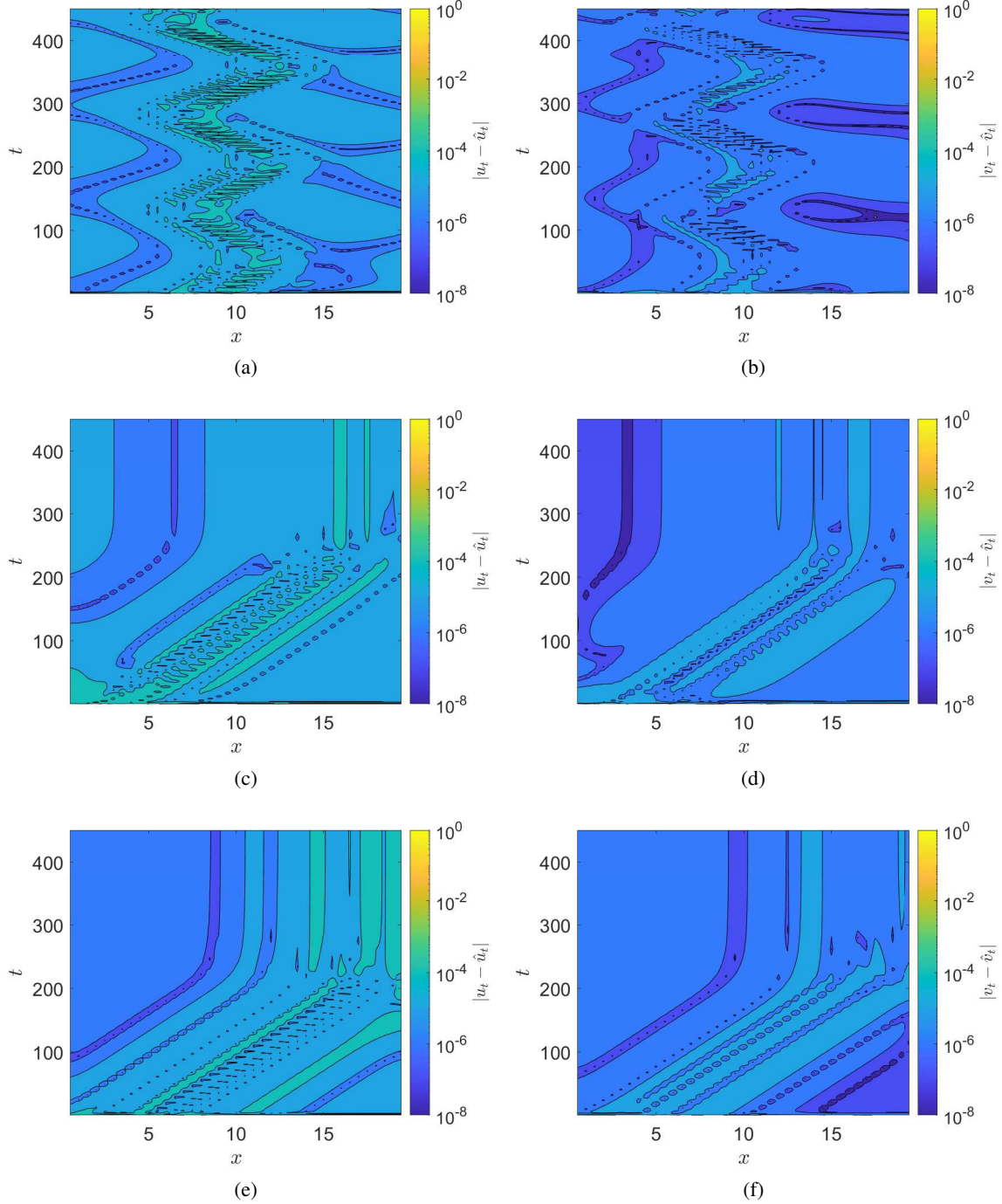


Figure 8: Contour plot for  $\|u_t - \hat{u}_t\|$  in the test dataset between the predicted time derivatives from the RPNN ( $\hat{u}_t$ ) without feature selection and the actual time derivatives  $u_t$  ((a), (c), and (e)) and for  $\|v_t - \hat{v}_t\|$  ((b), (d), and (f)) for different values of  $\varepsilon$ : (a) and (b)  $\varepsilon = 0.0114$  near the Andronov-Hopf point, (c), (d), and (e)  $\varepsilon = 0.4$ , (e) and (f)  $\varepsilon = 0.9383$  near the turning point.

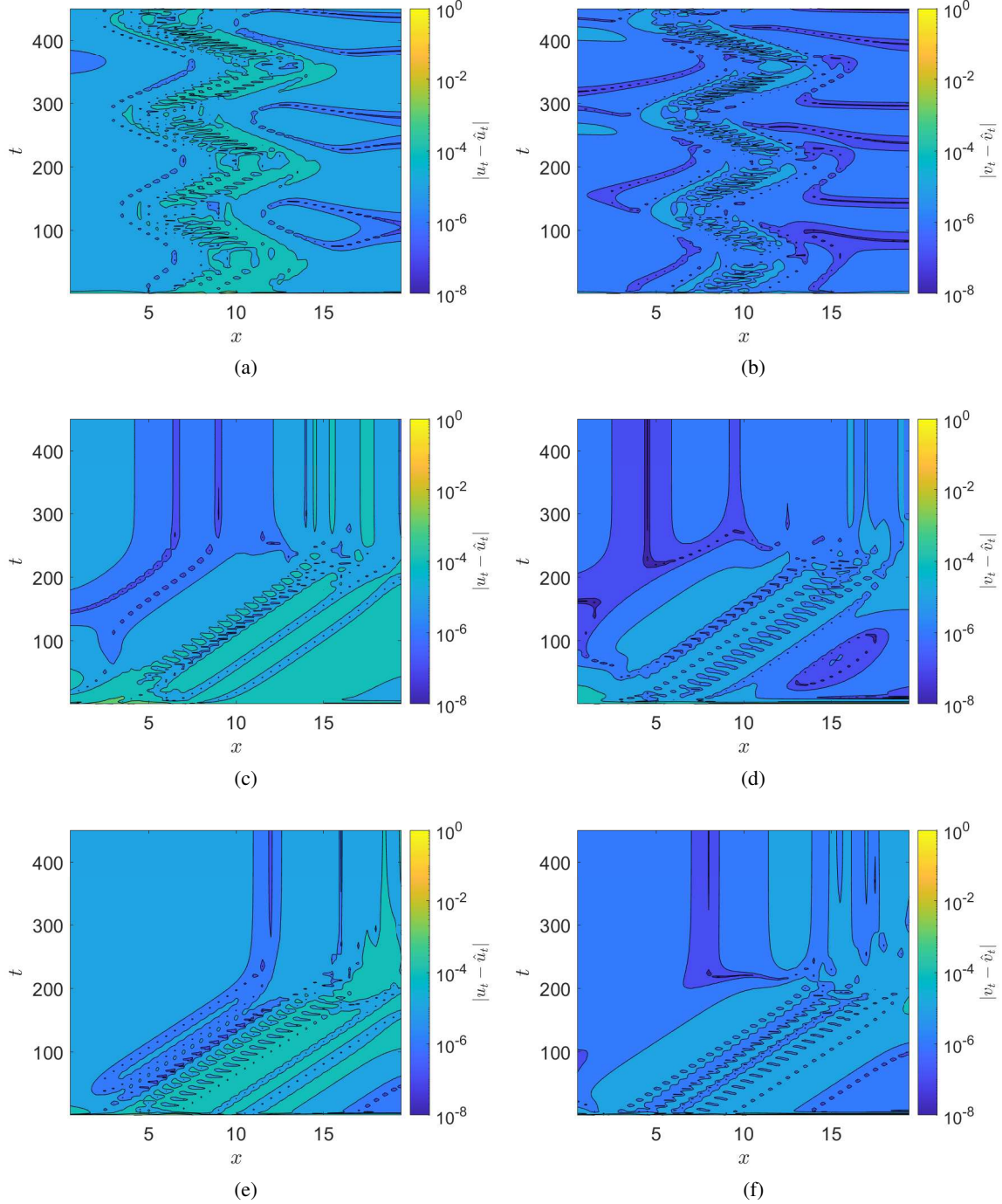


Figure 9: Contour plot for  $\|u_t - \hat{u}_t\|$  in the test dataset between the predicted time derivatives from the RPNN ( $\hat{u}_t$ ) with feature selection and the actual time derivatives  $u_t$  ((a), (c), and (e)) and for  $\|v_t - \hat{v}_t\|$  ((b), (d), and (f)) for different values of  $\varepsilon$ : (a) and (b)  $\varepsilon = 0.0114$  near the Andronov-Hopf point, (c), (d)  $\varepsilon = 0.4$ , (e) and (f)  $\varepsilon = 0.9383$  near the turning point.

test set				train set				
	MSE (u)	$L_{\inf}$ (u)	MSE (v)	$L_{\inf}$ (v)	MSE (u)	$L_{\inf}$ (u)	MSE (v)	$L_{\inf}$ (v)
<b>FNN</b>	7.90e-09	2.26e-02	1.56e-09	6.63e-03	1.31e-09	7.00e-03	2.78e-10	2.58e-03
<b>FNN with FS</b>	5.39e-08	2.93e-02	1.16e-08	7.65e-03	1.90e-08	2.64e-02	1.37e-09	4.70e-03
<b>ELM</b>	2.91e-08	2.98e-02	4.50e-10	2.22e-03	6.90e-09	2.37e-02	7.06e-11	9.40e-04
<b>ELM with FS</b>	7.10e-08	3.07e-02	1.73e-08	1.60e-02	2.16e-08	2.85e-02	6.30e-10	3.84e-03

Table 1: Mean-square and  $L_{\inf}$  errors between the predicted from the FNNs and RPNNs and the actual time derivatives of  $u$  and  $v$ .

$\varepsilon = 0.9383$  where the solutions are the embedded space is one dimensional line in a two dimensional space since time derivatives converges rapidly to zero (Figures 10(c), 10(e), 10(d) and 10(f)). The “good” subsets of the input data domain are presented in Table (2). As expected, the best candidate features are the  $(u, v, u_{xx})$  for  $u_t$  and  $(u, v, v_{xx})$  for  $v_t$  which are the only features that indeed appear in the closed form of the FHN PDEs. For the selection of the three parsimonious Diffusion Maps coordinates, we used the datafold package in python ([69]).

	$u_t = (\phi_1^u, \phi_2^u, \phi_3^u)$		$v_t = (\phi_1^v, \phi_2^v, \phi_3^v)$
Features	Sum Total Losses	Features	Sum Total Losses
<b>1d</b> $(u)$	4.3E-03	$(u)$	7.6E-03
<b>2d</b> $(u, v)$	6.37E-06	$(u, v)$	1.91E-05
<b>3d</b> $(u, v, u_{xx})$	2.77E-07	$(u, v, v_{xx})$	6.29E-07
<b>4d</b> $(u, v, u_x, u_{xx})$	1.03E-07	$(u, v, v_x, v_{xx})$	1.34E-07

Table 2: The “best” variables that can effectively parametrize the intrinsic coordinates  $((\phi_1^u, \phi_2^u, \phi_3^u)$  and  $(\phi_1^v, \phi_2^v, \phi_3^v)$ ) and the corresponding sums of total losses across all the values of the bifurcation parameter  $\varepsilon$ .

Finally, we repeated the same steps but now using as inputs in the FNNs and RPNNs the reduced input domain as obtained from the feature selection process, the bifurcation parameter. Figures (5(e)), (5(f)), (5(g)) and (5(h)) show the regression results of the two schemes. Table (1) summarizes the performance of the schemes on the training and the test set. The training phase of the FNN for  $\hat{u}_t$  stoped at 1000-th epoch and required 3 hours and 37 minutes with minimum tolerance set to  $1e-07$ . The training phase of the FNN for  $\hat{v}_t$  stoped at 1000-th epoch and required 4 hours and 19 minutes. Figures (7) and (9) illustrate the differences between the predicted from the FNNs and RPNNs with feature selection and the actual time derivatives. Hence, we have:

$$\begin{aligned} \frac{\partial u}{\partial t} &= \hat{F}^u(u, v, u_{xx}, \varepsilon), \\ \frac{\partial v}{\partial t} &= \hat{F}^v(u, v, v_{xx}, \varepsilon) \end{aligned} \quad (48)$$

where  $\hat{F}^u$  and  $\hat{F}^v$  are the outputs of the FNNs (or the RPNNs) and we perform Arc Length for  $\varepsilon$ , computing numerically the Jacobians of  $F^u$  and  $F^v$ . Thus, the data-driven bifurcation diagram with feature selection is shown in Figure 11. Now, using the FNNs, we estimated the Andronov-Hopf point at  $\varepsilon \approx 0.0195$  and the turning point at  $\varepsilon \approx 0.9762$ . Using the RPNNs, we estimated the Andronov-Hopf point at  $\varepsilon \approx 0.0192$  and the turning point at  $\varepsilon \approx 0.9752$ .

## 6 Conclusions

Buliding on previous efforts [29], we present a machine-learning methodology for constructing the coarse-bifurcation diagrams using fine scale simulations in space and time. The proposed approach is a three tier one. In the first step, we use non-linear manifold-learning and in particular Diffusion Maps to select the right coarse-scale observables that define the low-dimensional manifold on which the emergent dynamics evolve in the parameter space. At the second step, we learn the right-hand-side of the effective PDEs with respect to the coarse-scale observables; here we used FNNs and RPNNs (and in particular ELMs). Finally, based on the constructed black-box model, we construct the coarse-grained bifurcation diagrams exploiting the arsenal of numerical bifurcation. To demonstrate the approach, we used Lattice-Boltzmann simulations of the FitzHugh-Nagumo PDEs and compared the obtained bifurcation diagram with the one constructed directly by discretizing the PDEs with Finite-Differences.

The results show that the proposed machine-learning framework was able to identify a set of a coarse-scale variables

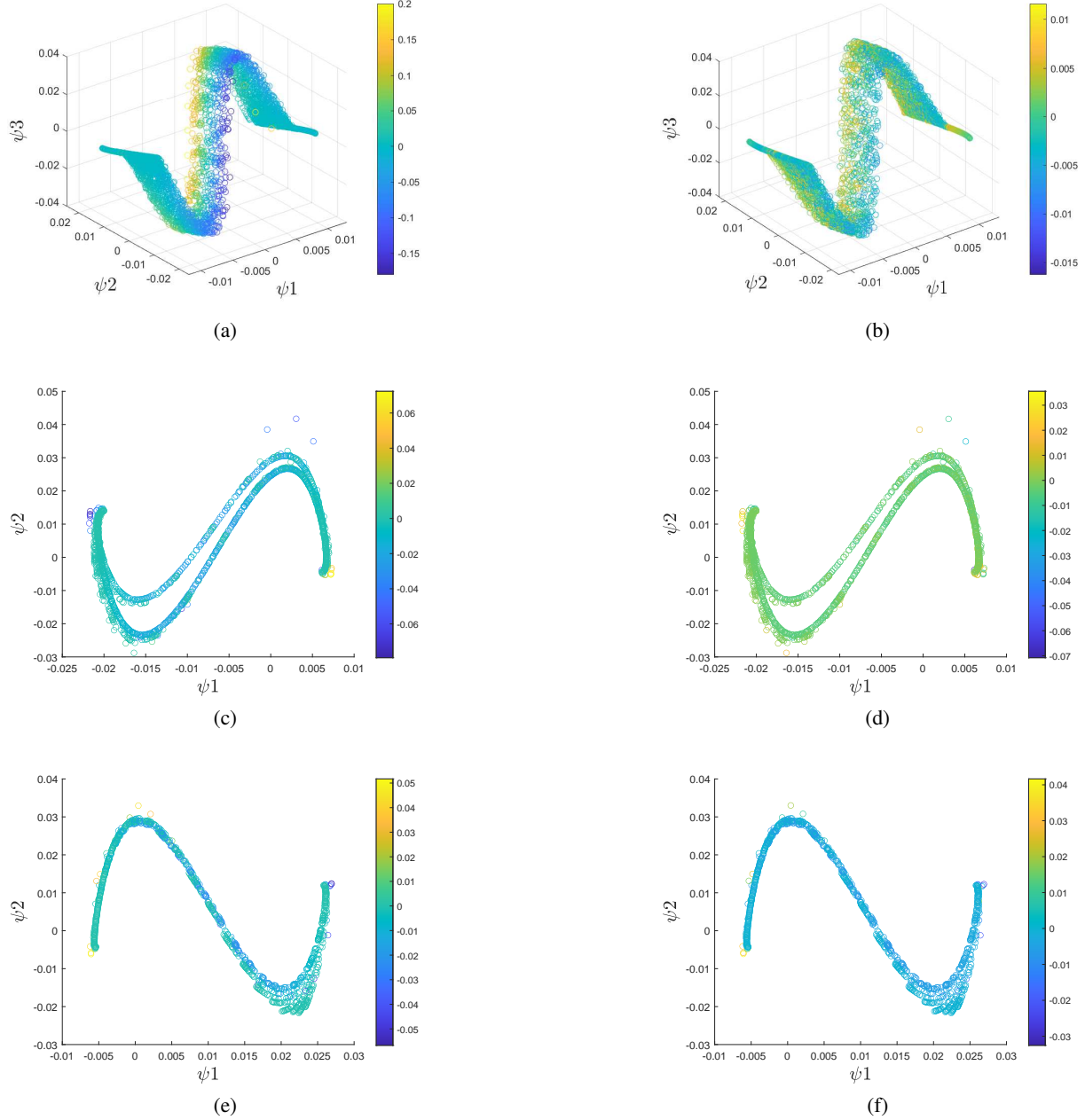


Figure 10: (a) and (b): The three parsimonious Diffusion Maps coordinates for  $\varepsilon = 0.01114$  near the Andronov-Hopf point. In this region the solutions are oscillating. (c) and (d): The two parsimonious Diffusion maps coordinates for  $\varepsilon = 0.4010$ . (e) and (f): The two parsimonious Diffusion maps coordinates for  $\varepsilon = 0.9383$  near the turning point. Colors represent  $u_t$  ((a), (c), (e)) and  $v_t$  ((b), (d), (f)).

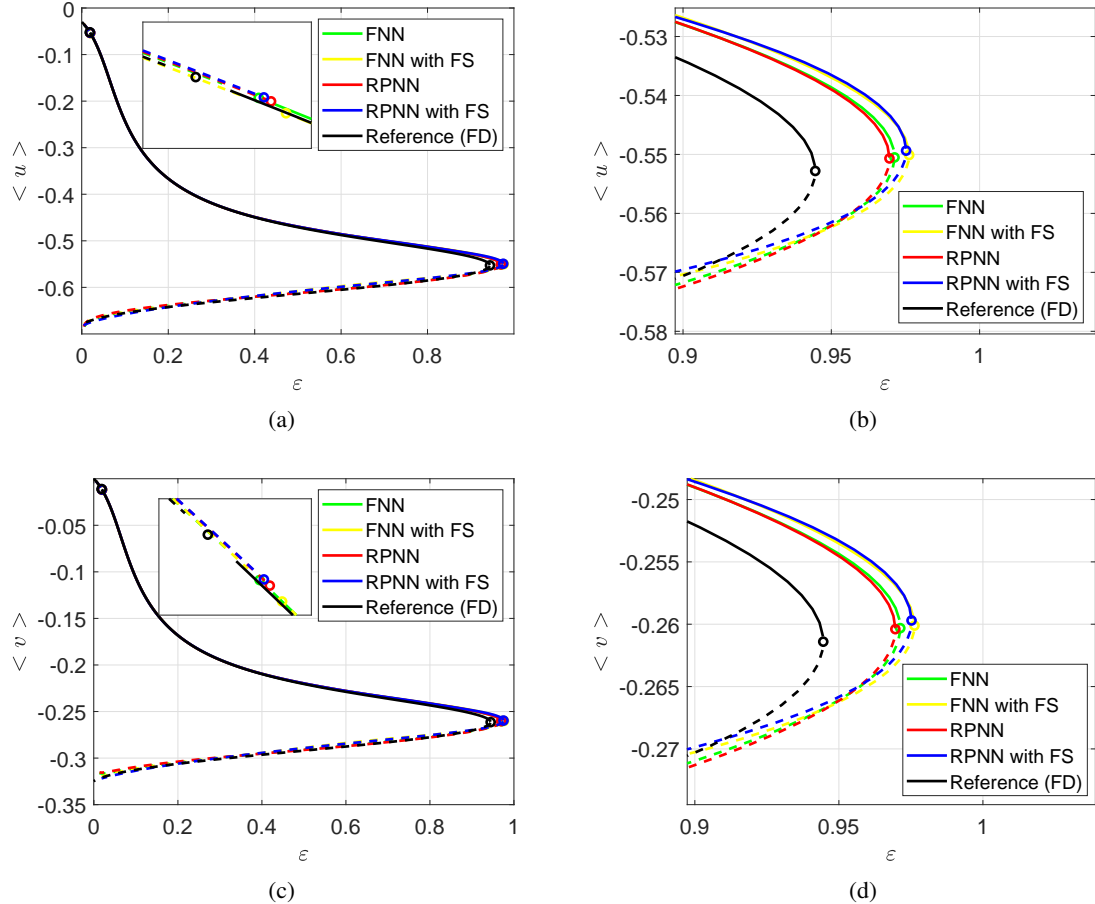


Figure 11: Reconstructed bifurcation diagram from the Lattice-Boltzmann simulations of the FHN dynamics with respect to  $\varepsilon$  with FNNs and RPNNs with feature selection. (a)  $\langle u \rangle$ ; the inset zooms near the Andronov-Hopf bifurcation point (b)  $\langle u \rangle$ ; the inset zooms near the turning Point, (c)  $\langle v \rangle$ ; the inset zooms near the Andronov-Hopf bifurcation point, (d)  $\langle v \rangle$ ; the inset zooms near the turning Point.

that are required to model the emergent dynamics and based on them to construct accurately the actual bifurcation diagram. In terms of approximation accuracy of the observed dynamics, both schemes (the FNNs and RPNNs) performed for all practical purposes equally. However, in terms of the computational cost in the training phase, the RPNN were more than 20 times faster compared that the FNNs as the training of RPNN requires just the solution of a regularized regression least-squares problem.

Here, we have focused on constructing black-box models of PDEs. The approach can be extended to construct “gray-box” models by incorporating information from the physics into the machine learning architecture [70]. Furthermore, based on previous efforts aiming at extracting normal forms of ODEs from data [71], the approach can be extended to discover normal forms of PDEs.

## Acknowledgments

This work was supported by the Italian program “Fondo Integrativo Speciale per la Ricerca (FISR)” - FISR2020IP 02893/B55F20002320001. Y.K. acknowledges partial support from US Department of Energy and the US Air Force Office of Scientific Research.

## References

- [1] George Em Karniadakis, Ioannis G Kevrekidis, Lu Lu, Paris Perdikaris, Sifan Wang, and Liu Yang. Physics-informed machine learning. *Nature Reviews Physics*, 3(6):422–440, 2021.
- [2] Michael Schmidt and Hod Lipson. Distilling free-form natural laws from experimental data. *science*, 324(5923):81–85, 2009.
- [3] Sifan Wang, Hanwen Wang, and Paris Perdikaris. Learning the solution operator of parametric partial differential equations with physics-informed deepnets. *Science Advances*, 7(40):eabi8605, 2021.
- [4] Nikola Kovachki, Zongyi Li, Burigede Liu, Kamyar Azizzadenesheli, Kaushik Bhattacharya, Andrew Stuart, and Anima Anandkumar. Neural operator: Learning maps between function spaces. *arXiv preprint arXiv:2108.08481*, 2021.
- [5] J.L. Hudson, M. Kube, R.A. Adomaitis, I.G. Kevrekidis, A.S. Lapedes, and R.M. Farber. Nonlinear signal processing and system identification: applications to time series from electrochemical reactions. *Chemical Engineering Science*, 45(8):2075–2081, 1990.
- [6] K. Krischer, R. Rico-Martinez, I. G. Kevrekidis, HH Rotermund, G. Ertl, and JL Hudson. Model identification of a spatiotemporally varying catalytic reaction. *Aiche JournalAiche Journal*, 39(1):89–98, JAN 1993 1993.
- [7] R. Rico-Martinez, J.S. Anderson, and I.G. Kevrekidis. Continuous-time nonlinear signal processing: a neural network based approach for gray box identification. In *Proceedings of IEEE Workshop on Neural Networks for Signal Processing*, pages 596–605, 1994.
- [8] J.S. Anderson, I.G. Kevrekidis, and R. Rico-Martinez. A comparison of recurrent training algorithms for time series analysis and system identification. *Computers & Chemical Engineering*, 20:S751–S756, 1996. European Symposium on Computer Aided Process Engineering-6.
- [9] R. González-García, R. Rico-Martínez, and I.G. Kevrekidis. Identification of distributed parameter systems: A neural net based approach. *Computers & Chemical Engineering*, 22:S965–S968, 1998. European Symposium on Computer Aided Process Engineering-8.
- [10] AP Alexandridis, CI Siettos, HK Sarimveis, AG Boudouvis, and GV Bafas. Modelling of nonlinear process dynamics using kohonen’s neural networks, fuzzy systems and chebyshev series. *Computers & Chemical Engineering*, 26(4-5):479–486, 2002.
- [11] Josh Bongard and Hod Lipson. Automated reverse engineering of nonlinear dynamical systems. *Proceedings of the National Academy of Sciences*, 104(24):9943–9948, 2007.
- [12] Steven L Brunton, Joshua L Proctor, and J Nathan Kutz. Discovering governing equations from data by sparse identification of nonlinear dynamical systems. *Proceedings of the national academy of sciences*, 113(15):3932–3937, 2016.
- [13] Ioannis G. Kevrekidis, C. William Gear, James M. Hyman, Panagiotis G. Kevrekidis, Olof Runborg, and Constantinos Theodoropoulos. Equation-free, coarse-grained multiscale computation: Enabling macroscopic simulators to perform system-level analysis. *Communications in Mathematical Sciences*, 1(4):715–762, 2003.
- [14] Ioannis G. Kevrekidis, C. William Gear, and Gerhard Hummer. Equation-free: The computer-aided analysis of complex multiscale systems. *AICHE Journal*, 50(7):1346–1355, 2004.
- [15] Alexei G. Makeev, Dimitrios Maroudas, and Ioannis G. Kevrekidis. “coarse” stability and bifurcation analysis using stochastic simulators: Kinetic monte carlo examples. *The Journal of Chemical Physics*, 116(23):10083–10091, June 2002.
- [16] C. I. Siettos, M. D. Graham, and I. G. Kevrekidis. Coarse brownian dynamics for nematic liquid crystals: Bifurcation, projective integration, and control via stochastic simulation. *The Journal of Chemical Physics*, 118(22):10149–10156, June 2003.
- [17] Radek Erban, Thomas A Frewen, Xiao Wang, Timothy C Elston, Ronald Coifman, Boaz Nadler, and Ioannis G Kevrekidis. Variable-free exploration of stochastic models: a gene regulatory network example. *The Journal of chemical physics*, 126(15):04B618, 2007.
- [18] Christophe Vandekerckhove, Ioannis Kevrekidis, and Dirk Roose. An efficient newton-krylov implementation of the constrained runs scheme for initializing on a slow manifold. *Journal of Scientific Computing*, 39(2):167–188, 2009.
- [19] Giovanni Samaey, Wim Vanroose, Dirk Roose, and Ioannis G Kevrekidis. Newton–krylov solvers for the equation-free computation of coarse traveling waves. *Computer Methods in Applied Mechanics and Engineering*, 197(43-44):3480–3491, 2008.

- [20] Giovanni Samaey and Wim Vanroose. An analysis of equivalent operator preconditioning for equation-free newton–krylov methods. *SIAM journal on numerical analysis*, 48(2):633–658, 2010.
- [21] C. I. Siettos, C. W. Gear, and I. G. Kevrekidis. An equation-free approach to agent-based computation: Bifurcation analysis and control of stationary states. *EPL (Europhysics Letters)*, 99(4):48007, August 2012.
- [22] R. R. Coifman, S. Lafon, A. B. Lee, M. Maggioni, B. Nadler, F. Warner, and S. W. Zucker. Geometric diffusions as a tool for harmonic analysis and structure definition of data: Diffusion maps. *Proceedings of the National Academy of Sciences*, 102(21):7426–7431, 2005.
- [23] Ronald R. Coifman and Stéphane Lafon. Diffusion maps. *Applied and Computational Harmonic Analysis*, 21(1):5–30, 2006. Special Issue: Diffusion Maps and Wavelets.
- [24] Boaz Nadler, Stéphane Lafon, Ronald R Coifman, and Ioannis G Kevrekidis. Diffusion maps, spectral clustering and reaction coordinates of dynamical systems. *Applied and Computational Harmonic Analysis*, 21(1):113–127, 2006.
- [25] Amit Singer, Radek Erban, Ioannis G Kevrekidis, and Ronald R Coifman. Detecting intrinsic slow variables in stochastic dynamical systems by anisotropic diffusion maps. *Proceedings of the National Academy of Sciences*, 106(38):16090–16095, 2009.
- [26] Seungjoon Lee, Ioannis G Kevrekidis, and George Em Karniadakis. A resilient and efficient cfd framework: Statistical learning tools for multi-fidelity and heterogeneous information fusion. *Journal of Computational Physics*, 344:516–533, 2017.
- [27] Maziar Raissi, Paris Perdikaris, and George Em Karniadakis. Inferring solutions of differential equations using noisy multi-fidelity data. *Journal of Computational Physics*, 335:736–746, 2017.
- [28] Maziar Raissi, Paris Perdikaris, and George Em Karniadakis. Machine learning of linear differential equations using gaussian processes. *Journal of Computational Physics*, 348:683–693, 2017.
- [29] Seungjoon Lee, Mahdi Kooshkbaghi, Konstantinos Spiliotis, Constantinos I. Siettos, and Ioannis G. Kevrekidis. Coarse-scale pdes from fine-scale observations via machine learning. *Chaos: An Interdisciplinary Journal of Nonlinear Science*, 30(1):013141, 2020.
- [30] C.J. Dsilva, R. Talmon, R.R. Coifman, and I.G. Kevrekidis. Parsimonious representation of nonlinear dynamical systems through manifold learning: A chemotaxis case study. *Applied and Computational Harmonic Analysis*, 44(3):759–773, 2018.
- [31] Alexander Holiday, Mahdi Kooshkbaghi, Juan M. Bello-Rivas, C. William Gear, Antonios Zagaris, and Ioannis G. Kevrekidis. Manifold learning for parameter reduction. *Journal of Computational Physics*, 392:419–431, 2019.
- [32] Boaz Nadler, Stéphane Lafon, Ronald R. Coifman, and Ioannis G. Kevrekidis. Diffusion maps - a probabilistic interpretation for spectral embedding and clustering algorithms. 2008.
- [33] Siyuan Gao, Gal Mishne, and Dustin Scheinost. Nonlinear manifold learning in functional magnetic resonance imaging uncovers a low-dimensional space of brain dynamics. *Human Brain Mapping*, 42, 06 2021.
- [34] Fadil Santosa and William W. Symes. Linear inversion of band-limited reflection seismograms. *SIAM Journal on Scientific and Statistical Computing*, 7(4):1307–1330, 1986.
- [35] Robert Tibshirani. Regression shrinkage and selection via the lasso. *Journal of the Royal Statistical Society. Series B (Methodological)*, 58(1):267–288, 1996.
- [36] Tin Kam Ho. Random decision forests. In *Proceedings of 3rd International Conference on Document Analysis and Recognition*, volume 1, pages 278–282 vol.1, 1995.
- [37] Tin Kam Ho. The random subspace method for constructing decision forests. *IEEE Transactions on Pattern Analysis and Machine Intelligence*, 20(8):832–844, 1998.
- [38] Carl Edward Rasmussen and Christopher K. I. Williams. *Gaussian Processes for Machine Learning (Adaptive Computation and Machine Learning)*. The MIT Press, 2005.
- [39] George V. Cybenko. Approximation by superpositions of a sigmoidal function. *Mathematics of Control, Signals and Systems*, 2:303–314, 1989.
- [40] Kurt Hornik, Maxwell Stinchcombe, and Halbert White. Multilayer feedforward networks are universal approximators. *Neural Networks*, 2(5):359–366, 1989.
- [41] Kurt Hornik, Maxwell Stinchcombe, and Halbert White. Universal approximation of an unknown mapping and its derivatives using multilayer feedforward networks. *Neural Networks*, 3(5):551–560, 1990.

- [42] Jooyoung Park and Irwin W. Sandberg. Universal approximation using radial-basis-function networks. *Neural Computation*, 3(2):246–257, 1991.
- [43] Moshe Leshno, Vladimir Ya Lin, Allan Pinkus, and Shimon Schocken. Multilayer feedforward networks with a nonpolynomial activation function can approximate any function. *Neural networks*, 6(6):861–867, 1993.
- [44] F. Dan Foresee and M.T. Hagan. Gauss-newton approximation to bayesian learning. In *Proceedings of International Conference on Neural Networks (ICNN'97)*, volume 3, pages 1930–1935 vol.3, 1997.
- [45] M.T. Hagan and M.B. Menhaj. Training feedforward networks with the marquardt algorithm. *IEEE Transactions on Neural Networks*, 5(6):989–993, 1994.
- [46] Andrew R Barron. Universal approximation bounds for superpositions of a sigmoidal function. *IEEE Transactions on Information theory*, 39(3):930–945, 1993.
- [47] Boris Igelnik and Yoh-Han Pao. Stochastic choice of basis functions in adaptive function approximation and the functional-link net. *IEEE Transactions on Neural Networks*, 6(6):1320–1329, 1995.
- [48] David Verstraeten, Benjamin Schrauwen, Michiel d’Haene, and Dirk Stroobandt. An experimental unification of reservoir computing methods. *Neural networks*, 20(3):391–403, 2007.
- [49] Herbert Jaeger. The “echo state” approach to analysing and training recurrent neural networks-with an erratum note. *Bonn, Germany: German National Research Center for Information Technology GMD Technical Report*, 148(34):13, 2001.
- [50] Guang-Bin Huang, Qin-Yu Zhu, and Chee-Kheong Siew. Extreme learning machine: theory and applications. *Neurocomputing*, 70(1-3):489–501, 2006.
- [51] Wolfgang Maass, Thomas Natschläger, and Henry Markram. Real-time computing without stable states: A new framework for neural computation based on perturbations. *Neural computation*, 14(11):2531–2560, 2002.
- [52] C. Van Der Malsburg. Frank Rosenblatt: Principles of neurodynamics: Perceptrons and the theory of brain mechanisms. In Günther Palm and Ad Aertsen, editors, *Brain Theory*, pages 245–248, Berlin, Heidelberg, 1986. Springer Berlin Heidelberg.
- [53] William B. Johnson and Joram Lindenstrauss. Extensions of Lipschitz mappings into a Hilbert space. *Contemporary Mathematics*, 26(1):189–206, 1984.
- [54] Dimitris Achlioptas. Database-friendly random projections: Johnson-Lindenstrauss with binary coins. *Journal of Computer and System Sciences*, 66(4):671–687, 2003.
- [55] Sanjoy Dasgupta and Anupam Gupta. An elementary proof of a theorem of Johnson and Lindenstrauss. *Random Structures & Algorithms*, 22(1):60–65, 2003.
- [56] Santosh S. Vempala. *The random projection method*, volume 65. American Mathematical Soc., 2005.
- [57] Jianzhong Wang. Geometric structure of high-dimensional data. In *Geometric Structure of High-Dimensional Data and Dimensionality Reduction*, pages 51–77. Springer, 2012.
- [58] Raja Giryes, Guillermo Sapiro, and Alex M Bronstein. Deep neural networks with random gaussian weights: A universal classification strategy? *IEEE Transactions on Signal Processing*, 64(13):3444–3457, 2016.
- [59] Richard FitzHugh. Impulses and physiological states in theoretical models of nerve membrane. *Biophysical journal*, 1(6):445–466, 1961.
- [60] Constantinos Theodoropoulos, Yue-Hong Qian, and Ioannis G. Kevrekidis. “coarse” stability and bifurcation analysis using time-steppers: A reaction-diffusion example. *Proceedings of the National Academy of Sciences*, 97(18):9840–9843, 2000.
- [61] Shiyi Chen and Gary D. Doolen. Lattice boltzmann method for fluid flows. *Annual Review of Fluid Mechanics*, 30(1):329–364, 1998.
- [62] Julia M. Yeomans. The lattice boltzmann equation for fluid dynamics and beyond. *Physics Today*, 55(12):58–60, 2002.
- [63] P. L. Bhatnagar, E. P. Gross, and M. Krook. A model for collision processes in gases. i. small amplitude processes in charged and neutral one-component systems. *Phys. Rev.*, 94:511–525, May 1954.
- [64] P. Bhatnagar, E. Gross, and Max Krook. A model for collision processes in gases. *Physical Review*, 94(3):511, 1954.
- [65] Y.H. Qian and S.A. Orszag. Scalings in diffusion-driven reaction  $a + b \rightarrow c$ : Numerical simulations by lattice bgk models. *J Stat Phys*, 81:237–253, 1995.

- [66] Tony F. C. Chan and H. B. Keller. Arc-length continuation and multigrid techniques for nonlinear elliptic eigenvalue problems. *SIAM Journal on Scientific and Statistical Computing*, 3(2):173–194, 1982.
- [67] Roland Glowinski, Herbert B. Keller, and Laure Reinhart. Continuation-conjugate gradient methods for the least squares solution of nonlinear boundary value problems. *Siam Journal on Scientific and Statistical Computing*, 6:793–832, 1985.
- [68] Willy Govaerts. Numerical methods for bifurcations of dynamical equilibria. 1987.
- [69] Daniel Lehmberg, Felix Dietrich, Gerta Köster, and Hans-Joachim Bungartz. datafold: data-driven models for point clouds and time series on manifolds. *Journal of Open Source Software*, 5:2283, 07 2020.
- [70] Robert J Lovelett, Jose L Avalos, and Ioannis G Kevrekidis. Partial observations and conservation laws: Gray-box modeling in biotechnology and optogenetics. *Industrial & Engineering Chemistry Research*, 59(6):2611–2620, 2019.
- [71] Or Yair, Ronen Talmon, Ronald R Coifman, and Ioannis G Kevrekidis. Reconstruction of normal forms by learning informed observation geometries from data. *Proceedings of the National Academy of Sciences*, 114(38):E7865–E7874, 2017.

This figure "overview.png" is available in "png" format from:

<http://arxiv.org/ps/2201.13323v1>